Atmos. Chem. Phys., 25, 14099–14129, 2025
https://doi.org/10.5194/acp-25-14099-2025

Atmospheric Chemistry and Physics
Open Access
EGU

Advances in CALIPSO (IIR) cirrus cloud property retrievals – Part 2: Global estimates of the fraction of cirrus clouds affected by homogeneous ice nucleation

David L. Mitchell[1] **and Anne Garnier**[2]

[1]Desert Research Institute, Reno, NV 89512-1095, USA
[2]RSES, Analytical Mechanics Associates, Hampton, VA 23666, USA

Correspondence: David L. Mitchell (david.mitchell@dri.edu)

Received: 4 December 2024 – Discussion started: 12 December 2024
Revised: 24 July 2025 – Accepted: 24 July 2025 – Published: 29 October 2025

Abstract. Cirrus clouds can form through two ice nucleation pathways (homo- and heterogeneous ice nucleation; henceforth hom and het, respectively) that result in very different cloud physical and radiative properties. While important to the climate system, they are poorly understood due to lack of knowledge on the relative roles of hom and het. This study differs from earlier relevant studies by estimating the relative radiative contribution of hom-affected cirrus clouds. Here, we employ new global retrievals (described in Part 1: Mitchell et al., 2025; henceforth M2025) of cirrus cloud ice particle number concentration, effective diameter (D_e), ice water content (IWC), shortwave extinction coefficient (α_{ext}), optical depth (τ) and cloud radiative temperature based on Imaging Infrared Radiometer (IIR) and Cloud and Aerosol Lidar with Orthogonal Polarization (CALIOP) co-located observations onboard Cloud-Aerosol Lidar and Infrared Pathfinder Satellite Observation (CALIPSO). Transition from het dominated to hom-affected regimes are identified using α_{ext} and D_e. Over oceans outside the tropics in winter, the zonal fraction of hom-affected cirrus generally ranges between 20 % and 35 %, with comparable contributions from in situ and warm base cirrus. Using τ distributions to establish a proxy for net cloud radiative effect (CRE), the τ-weighted fraction for hom-affected cirrus over oceans outside the tropics during winter was > 50 %, indicating that hom cirrus play an important role in climate. Using these retrievals (including those relating to the cloud geometric thickness), a conceptual model of cirrus cloud characterization is proposed.

1 Introduction

Clouds are important due to their critical role in the Earth's radiation budget (e.g., Kiehl and Trenberth, 1997) and need to be realistically predicted in climate models in terms of their coverage, altitude, temperature and optical thickness or depth to accurately predict climate change (e.g., Stephens, 2005). The microphysical and radiative properties of cirrus clouds are poorly understood in large part due to two pathways or mechanisms through which the cirrus clouds form: heterogeneous ice nucleation (henceforth het) and homogeneous ice nucleation (henceforth hom). Since het activates before hom begins, this can result in two types of cirrus clouds: (1) cirrus formed through het (i.e., het cirrus) and (2) cirrus formed through a combination of het and hom (i.e., hom cirrus). Since hom generally results in relatively high concentrations of ice crystals (which can in turn affect their sizes and the cloud ice water content (IWC)) while het produces relatively few, the microphysical and radiative properties of het and hom cirrus could strongly differ (Barahona and Nenes, 2009; Mitchell et al., 2018; henceforth M2018).

Cirrus clouds have also been classified in terms of their origin as (1) in situ cirrus and (2) liquid origin cirrus (LOC) (e.g., Krämer et al., 2016; Luebke et al., 2016; Dekoutsidis et al., 2023), with LOC associated with cloudy air advected from lower levels ($T > 235$ K) that is typically near ice saturation and completely glaciated by the Wegener–Bergeron–Findeisen process when this air enters the cirrus temperature regime ($T \leq 235$ K; Luebke et al., 2016; Costa et al., 2017; Avery et al., 2020; Mitchell and d'Entremont, 2012). How-

ever, at high vertical velocities liquid cloud droplets may be advected into the cirrus regime where they immediately freeze homogeneously (e.g., Rosenfeld and Woodley, 2000). LOC are expected to result from deep convection that produces anvil cirrus and may occur in frontal systems where a "conveyor belt" of condensate is advected from warmer levels into cirrus clouds. In situ cirrus clouds are not subject to condensate advection from levels below the 235 K isotherm, and they form and grow within an ice cloud only environment. Using aircraft measurements from many field campaigns, Luebke et al. (2016) found that cirrus IWC was higher in LOC while differences between ice particle number concentration N_i and D_m were similar for a given altitude, where D_m corresponds to the ice particle size distribution (PSD) bin size where the maximum amount of ice mass is located. This study utilizes a similar cirrus cloud classification, comparing relative differences in N_i, effective diameter D_e and IWC regarding in situ cirrus and an approximation for LOC clouds (as described in Sect. 2.1).

Since this study estimates the fraction of cirrus clouds strongly affected by hom, we briefly review similar estimates from modeling and observational studies here. Some studies using global climate models (GCMs) have predicted the role of hom relative to het. Using the Community Atmosphere Model Version 5 (CAM5) with the Liu and Penner (2005) ice nucleation scheme, Gettelman et al. (2010), Liu et al. (2012), Gettelman et al. (2012), and Penner et al. (2015) found that het prevailed in the northern hemisphere (NH) outside the tropics, with hom prevailing in the southern hemisphere (SH) and in the tropics. Using the ECHAM6-HAM2 GCM, Gasparini and Lohmann (2016) found hom was only relevant near the tropopause over mountainous terrain in the NH and SH outside the tropics. Muench and Lohmann (2020) used this same GCM but without the treatment for orographic gravity waves (OGWs) used in Gasparini and Lohmann (2016). Their results regarding hom and het were similar to the CAM5 studies, with het prevailing over hom in the NH outside the tropics. However, hom resulting from cloud droplet freezing dominated ice production in the lower part of cirrus clouds at all latitudes, a result not found in a more detailed cloud process model (Lüttmer et al., 2025). The dominance of het relative to hom in the NH outside the tropics is common to all these studies (at least in the upper cirrus cloud), and this is predicted from the higher mineral dust concentrations in the NH, which are higher due to the much greater land area. This prediction was recently validated by Froyd et al. (2022) where global in situ measurements of the upper troposphere (UT) mineral dust concentration initialized a detailed cirrus-formation model that predicted the relative contributions of het and hom cirrus during four field campaigns that each traversed the world from pole-to-pole. Finally, Barahona et al. (2017) simulated hom and het in cirrus clouds using a GCM at 100 km horizontal resolution. However, standard deviations in vertical velocities (w), σ_w, were calculated at 7 km horizontal resolution in a separate simulation to drive ice nucleation processes in the lower resolution simulation. Results show that the frequency of hom cirrus clouds was highest in the tropics, intermediate in the SH and lowest in the NH, with hom cirrus highest during winter outside the tropics in both hemispheres due to colder temperatures. However, at high latitudes (especially in the Arctic), the fraction of hom cirrus was relatively low.

It is possible that hom plays a larger role in the NH than currently predicted in most climate models having explicit microphysics. For example, the satellite remote sensing study by Sourdeval et al. (2018) shows that N_i in cirrus clouds ($T < 235$ K) outside the tropics is relatively high during the NH and SH winter seasons, with relatively low N_i for $T > 235$ K. Highest N_i during winter was also observed in the cirrus cloud remote sensing study of M2018, which was limited to in situ cirrus clouds. These studies also found N_i outside the tropics ($\pm 30°$ latitude) was higher over mountainous terrain, attributing this to mountain-induced wave clouds having relatively strong and sustained updrafts (and thus greater cooling rates producing high supersaturations) conducive for hom. This was also observed in the satellite remote sensing study of Gryspeerdt et al. (2018) that explained the higher N_i over mountainous terrain in a similar way. Sedimenting ice crystals originating near cloud top may promote reduced N_i at lower levels by lowering the relative humidity with respect to ice (RH_i) there and "quenching" hom (Spichtinger and Gierens, 2009a), which is consistent with Fig. 10 in M2018. Aircraft measurements also underscore the importance of hom. By developing an analysis scheme sensitive to hom and het influences, Patnaude and Diao (2020) and Ngo et al. (2024) found evidence that both mechanisms are important in cirrus cloud formation, depending on environmental factors.

M2018 found that N_i was relatively high at high latitudes, mostly over land. This can be partly explained by the relatively low concentrations of ice nucleating particles (INPs), measured or inferred, over the Southern Ocean (Vergara-Temprado et al., 2018; McCluskey et al., 2018; Carlsen and David, 2022) and in the Arctic, especially when snow and sea ice cover is more extensive (Creamean et al., 2018; Carlsen and David, 2022). That is, when N_i produced by het is relatively low, the ice surface area produced for vapor removal is often inadequate for preventing the RH_i from climbing and reaching the hom threshold in a cirrus cloud updraft, generally resulting in higher N_i produced by hom (Krämer et al., 2016). Results similar to M2018 over the Southern Ocean are shown in Fig. 1 of Gryspeerdt et al. (2018).

As in M2018, the new Cloud-Aerosol Lidar and Infrared Pathfinder Satellite Observation (CALIPSO) satellite retrieval of D_e, N_i and IWC presented in Part 1 (Mitchell et al., 2025; henceforth M2025) uses the Imaging Infrared Radiometer (IIR) and Cloud and Aerosol Lidar with Orthogonal Polarization (CALIOP). The new retrievals of D_e, N_i, and IWC are based on an extended set of aircraft measurements. Whereas M2018 had several sets of retrievals for sev-

eral independent formulations, M2025 established a unique retrieval scheme which combines various formulations according to temperature and latitude. Nevertheless, the general findings from M2018 referred to above still stand.

In Sect. 2, we give an overview of the new retrievals based on M2025. Our cirrus cloud sampling is discussed, and we describe why $0.3 < \tau < 3.0$, where τ is visible optical depth, may be the most radiatively representative τ category for all cirrus clouds. In Sect. 3, we present the rationale for the identification of hom-affected cirrus clouds and a method for quantifying the fraction of hom-affected cirrus clouds is developed and the results are discussed. In Sect. 4, we synthesize results from this and previous studies to propose a conceptual model for characterizing cirrus clouds. This work is related to the treatment of cirrus clouds in Earth system models and cirrus cloud thinning in Sect. 5. A summary and conclusions are given in Sect. 6.

2 CALIPSO retrievals

2.1 Cloud sampling

As described in Part 1 (M2025), the CALIPSO retrieval uses IIR passive observations at 10.6 and 12.05 µm with description of the atmospheric column informed by perfectly collocated CALIOP observations. Results presented in this study are based on CALIPSO data during 2008, 2010, 2012 and 2013. Microphysical properties are retrieved for atmospheric columns that contain only one semi-transparent ice cloud layer that does not fully attenuate the CALIOP laser beam to ensure that cloud base is detected. We also require the cloud layer to be classified as ice with high confidence by the CALIOP ice/water phase algorithm (Avery et al., 2020). The CALIOP in-cloud 532 nm attenuated backscatter profiles with temperatures from MERRA-2 re-analyses (Gelaro et al., 2017) allows one to estimate the cloud layer radiative temperature, T_r (Garnier et al., 2021), and cirrus clouds are defined as those ice clouds having a $T_r \leq 235$ K. The upper range of optical depth for semi-transparent single-layer cirrus clouds is approximately 3. The lower range is driven by retrieval uncertainties. In earlier work (M2018), global retrievals over both oceans and land have been in clouds having a CALIOP 532 nm layer integrated attenuated backscatter (IAB) larger than 0.01 sr^{-1}, generally corresponding to clouds with visible optical depth $\tau > 0.3$. These clouds will be hereafter called "thick" cirrus clouds (see Table 1). However, over oceans, uncertainties are lower due to the absence of highly variable land surface emissivities, allowing all cirrus clouds with valid retrieved effective emissivities at both 10.6 and 12.0 µm to be considered, yielding $\tau > \sim 0.01$ (M2025).

The geographical distribution of the cirrus cloud sampling is shown in Fig. A1 in Appendix A. In M2018, the sampled cirrus clouds were in situ cirrus clouds having base temperature, T_{base}, colder than 235 K. In this work, we take advantage of the improved ice/water phase assignment in the Version 4 CALIOP products to also include cirrus clouds with T_{base} warmer than 235 K (and T_r colder than 235 K), hereafter called warm base cirrus clouds or WBC clouds. Even though these WBC clouds are identified as high confidence ice cloud layers by CALIOP, this assessment does not rule out the possibility of liquid droplets in the lower part of the layer. This classification method is an attempt to qualitatively contrast the properties of in situ and LOC clouds, using WBC as a proxy for LOC clouds. A similar approach was used in Gasparini et al. (2018). This approximation may underestimate LOC clouds (overestimating in situ cirrus) since cloud condensate from below the 235 K isotherm may be advected across this isotherm upwind of the CALIOP nadir view when there is no cloud at nadir below this isotherm. In this case the cloud would be mistakenly classified as in situ cirrus. On the other hand, the modeling study by Wernli et al. (2016) estimates that approximately 50 % of in situ cirrus clouds occur on top of LOC, indicating a strong dynamical linkage. Relative to an air parcel back trajectory analysis as used in Wernli et al. (2016) and other LOC studies cited below, our approach should underestimate in situ cirrus if there is no clear layer separating in situ from WBC clouds. This classification scheme is evaluated in Appendix A in Figs. A2 and A3. Figure A2 shows the dependence of the in situ fraction on temperature, where this fraction is ~ 0.5 (indicating a transition from in situ to WBC) at approximately 227 K over oceans when all clouds are considered. In the LOC studies by Dekoutsidis et al. (2023) and Luebke et al. (2016), which are both based on the same field campaign, this transition occurs around 221 K and between 218–222 K, respectively. This suggests that the WBC approximation overestimates the in situ fraction somewhat (shifting the transition temperature by ~ 6 K relative to these measurement-based studies), but that WBC may still serve as a qualitative proxy for LOC. The blue curves in Fig. A3 indicate that while WBC clouds have relatively higher IWCs, the main difference between them and in situ cirrus clouds is the greater ice water path (IWP) and τ associated with WBC clouds.

2.2 Realism of the CALIPSO cloud sampling for representing cirrus clouds

As in M2018, global retrievals over both oceans and land are in thick clouds having $\tau > \sim 0.3$, and we are now sampling both in situ cirrus and WBC clouds. This raises the question: "Is this subcategory of cirrus cloud adequate for testing cirrus clouds in climate models?" It was argued in Sect. 6.3 of M2018 that cirrus clouds in this τ range should dominate the overall cirrus cloud net radiative forcing, but more can be said about this. Table 4 in Hong et al. (2016) gives global mean top-of-atmosphere net ice cloud radiative effect (CRE) values for the following five τ categories: $\tau < 0.03$; $0.03 < \tau < 0.3$; $0.3 < \tau < 3.0$; $3 < \tau < 20$; $\tau > 20$. The corresponding net CRE values in W m^{-2} are:

Table 1. Notations used for CALIOP retrievals of cirrus clouds. Both in situ cirrus and warm base cirrus (WBC) clouds are included in the τ categories below unless otherwise indicated.

Notation	Definition or interpretation
T_{top}, T_{base}	Temperature at cloud top, temperature at cloud base
T_r	Cloud layer radiative temperature, on average in the middle between T_{top} and T_{base}.
τ	Visible cloud optical depth
IAB	CALIOP 532 nm layer integrated attenuated backscatter
Thin cirrus	IAB $< 0.01\ sr^{-1}$ $\sim 0.01 < \tau < \sim 0.3$: optically thin cirrus including some subvisible cirrus*
Thick cirrus	IAB $> 0.01\ sr^{-1}$ $\sim 0.3 < \tau < \sim 3$: optically thick cirrus, but semi-transparent to the lidar
All cirrus	$\sim 0.01 < \tau < \sim 3$; includes optically thin and thick cirrus clouds

* Subvisible cirrus ($\tau < 0.03$).

0.05, 0.96, 4.98, −0.49 and −0.43. These CRE values are weighted by ice cloud frequency of occurrence. Relative contributions of net CRE can be calculated by taking absolute values, in which case ice clouds having $0.3 \leq \tau \leq 3.0$ contribute 72 % of the total "absolute" CRE. Moreover, the global mean net CRE for all ice cloud categories in their Table 4 was $5.07\ W\ m^{-2}$ whereas the global mean net CRE for $0.3 \leq \tau \leq 3.0$ is $4.98\ W\ m^{-2}$, further suggesting that this thick cloud category is representative for all ice clouds. However, Hong et al. (2016) addressed all ice clouds (i.e., $T_r < 273$ K) whereas our study addresses only cirrus clouds ($T_r \leq 235$ K).

To further investigate this question for our cirrus sampling, we examine the distributions of retrieved τ (M2025) over oceans for the high- and midlatitudes and the tropics. The tropics are defined here as ±30°, while the mid- and high latitudes are 30–60 and 60–90° in each hemisphere, respectively. The τ distributions are built using bins equal to 0.1 in $\log(\tau)$ space. The number of IIR $1\ km^2$ cloudy pixels, p and the product $p \times \tau$, are plotted against τ in Fig. 1. This is done over oceans for all sampled cirrus clouds and for thick clouds that have lower retrieval uncertainties. The $p \times \tau$ product serves as a proxy for the radiative impact of cirrus clouds since τ and frequency of occurrence are the principal factors determining CREs. The right-hand panels in Fig. 1 show the cumulative distributions over τ (panel b) and for this proxy or radiative weighting (panel d). The cumulative distributions are normalized with respect to all cirrus clouds sampled. The cumulative distributions for thick clouds indicate that cirrus clouds having $\tau > \sim 0.3$ represent 31 % to 48 % (depending on latitude band) of the cirrus clouds sampled. However, they represent 78 % to 87 % of the radiative weight for all cirrus clouds sampled (i.e., cirrus clouds having $\tau < 0.3$ represent 13 % to 22 % of the radiative weight). This compares favorably with results from Hong et al. (2016) described above, where the ice cloud CRE fraction for $\tau < 0.3$ relative to $\tau < 3$ is 0.17, or 17 %. The occurrence frequency of cirrus having $\tau > 3$ is negligible here because only clouds that are semi-transparent to CALIOP are sampled.

2.3 Global maps of cirrus cloud properties

Global maps for December–January–February (DJF) and June–July–August (JJA) during 2008, 2010, 2012 and 2013 are shown for median N_i, D_e, IWC and cirrus cloud T_r for thick cirrus clouds (i.e., $\sim 0.3 < \tau < \sim 3$) in Figs. 2, 3, 4 and 5, respectively. Global maps for the two other seasons are given in the Supplement as Figs. S1 to S4. From Sect. 2.2, this sampling criteria appears to provide cloud property values of cirrus clouds whose radiative properties are representative of all cirrus clouds.

Relatively high N_i are found at high latitudes over land, as well as over mountainous regions in the midlatitudes, especially during winter. These observations appear consistent with hom since hom tends to produce higher N_i in stronger updrafts (e.g., OGWs induced by mountains) and during winter (Joos et al., 2014). The seasonal dependence of N_i in Fig. 2 was also found by Sourdeval et al. (2018, their Fig. 8) at mid-to-high latitudes for winter vs. summer. The regions with large N_i in the tropics in Sourdeval et al. (2018) are absent in Fig. 2 possibly because thick cirrus here have $\tau < \sim 3$ and thus deep convective cores (where hom is often active) are not sampled.

For a given season, regions having relatively high N_i in Fig. 2 have relatively small D_e in Fig. 3. An exception is in the tropical western Pacific during winter where D_e is relatively small and N_i is relatively low. The deepest convection occurs in this region during winter (Danielsen, 1993), producing the coldest cloud top temperatures where ice crystal growth rates are bound to be minimal, probably resulting in smaller D_e. This phenomenon is more evident in Fig. 4, showing retrieved median IWCs, where IWC is lowest during winter in the tropical western Pacific due to these minimal temperatures. The correspondence between T_r (Fig. 5) and IWC (Fig. 4) is clearly seen as expected from the Clausius–Clapeyron equation.

Figures S5 and S6 show global maps of median N_i and D_e for in situ cirrus clouds only, where N_i is higher and D_e considerably smaller relative to Figs. 2 and 3 (where WBC are included). To interpret these figures, microphysical properties of in situ cirrus and WBC clouds are investigated in

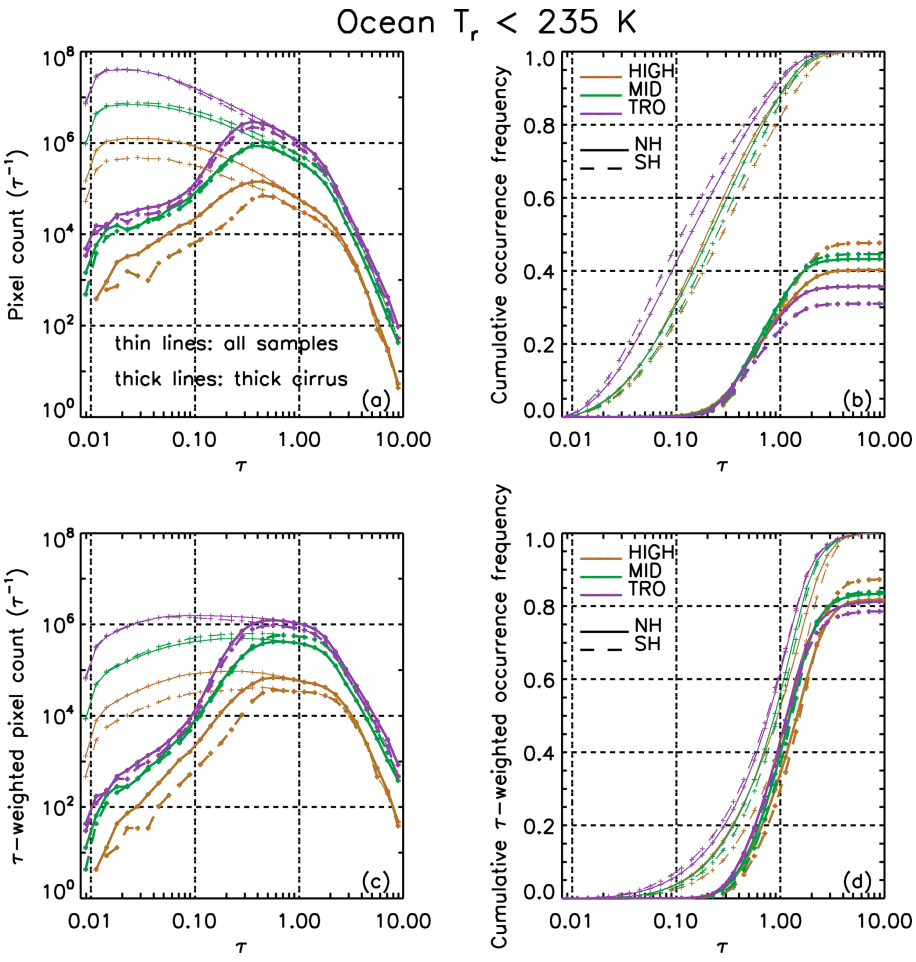

Figure 1. Panels **(a)** and **(b)** show IIR cirrus sampling statistics during 2008, 2010, 2012 and 2013 over visible optical depth (τ) while panels **(c)** and **(d)** show the same distribution of sampled pixels multiplied by τ. All samples have a cloud radiative temperature $T_r \leq 235$ K for the tropics (purple), midlatitudes (green) and high latitudes (brown). Solid and dashed patterns refer to the NH and SH, respectively. The product of the number of IIR pixels $\times\ \tau$ is a proxy for the radiative impact of cirrus clouds. The thin curves indicate all IIR samples while the thicker curves are for the optically thick clouds. Panels **(b)** and **(d)** show the cumulative distributions. The IIR pixels count is normalized per τ bin size. Retrievals are only over oceans to minimize uncertainties at the lowest τ.

Fig. A3. Although corresponding to a specific season and latitude zone, these Fig. A3 results are globally representative. Median D_e increases as T_r increases, with no marked difference between in situ and WBC cirrus clouds at a given T_r. This suggests that the D_e differences seen between Fig. 3 (for thick WBC and in situ cirrus) and the thick in situ cirrus in Fig. S6 (residing at a lower T_r on average) are due to temperature differences. Temperature could also be a factor in explaining the lower N_i in Fig. 2 (for thick WBC and in situ cirrus) relative to the thick in situ clouds in Fig. S5, since the latter tend to form at lower temperatures (Fig. A2) and hom depends strongly on temperature (e.g., Lamb and Verlinde, 2011). Figure A3 shows that both the geometric thickness and the equivalent thickness seen by IIR are on average greater for WBC clouds than for in situ cirrus clouds. This is the main reason that IWP and τ tend to be substantially greater for WBC clouds. Finally, IWC and N_i are both higher in WBC, in agreement with Luebke et al. (2016), only when clouds with $\tau < \sim 0.3$ are included (blue curves). Figure A3 highlights the importance of cloud sampling in optically thick vs. thin cirrus when interpreting cirrus cloud field campaign measurements of N_i and IWC, and ultimately in terms of the contribution of het and hom to cloud formation.

3 Contribution of hom-affected cirrus clouds

3.1 Sensitivity of cirrus cloud physical properties to hom

The main purpose of this section is to justify the use of the extinction coefficient α_{ext} as a means of separating cirrus clouds formed primarily through het from those formed primarily through hom. As discussed in M2025, when all IIR samples over oceans were used ($\sim 0.01 < \tau < \sim 3$) retrieved median N_i, R_v (mean volume radius), and IWC were in rea-

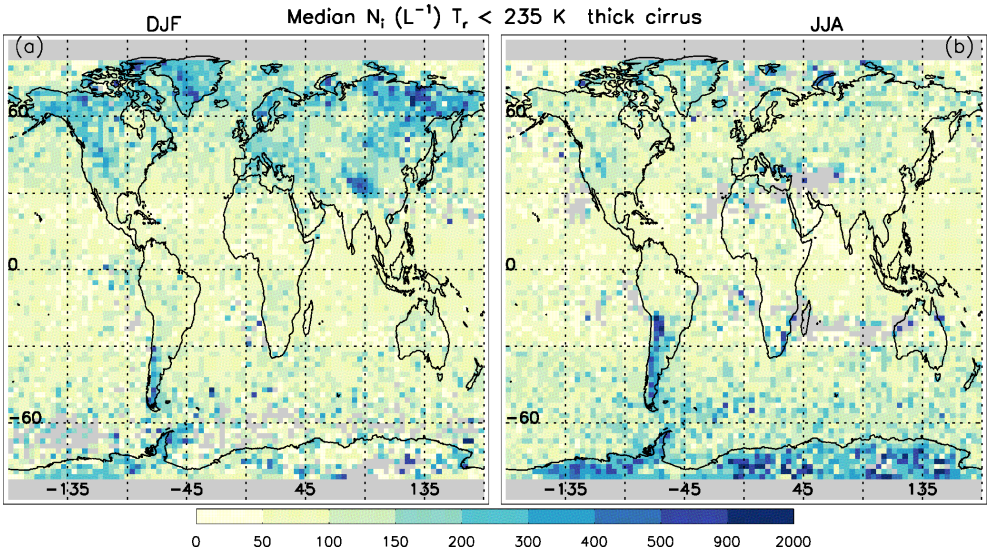

Figure 2. Global-seasonal maps of the median ice particle number concentration N_i for thick cirrus ($\sim 0.3 < \tau < \sim 3$) that include both WBC and in situ cirrus clouds. The color legend gives N_i in L^{-1}. The two panels are for **(a)** December–January–February (DJF) and **(b)** June–July–August (JJA) during 2008, 2010, 2012 and 2013.

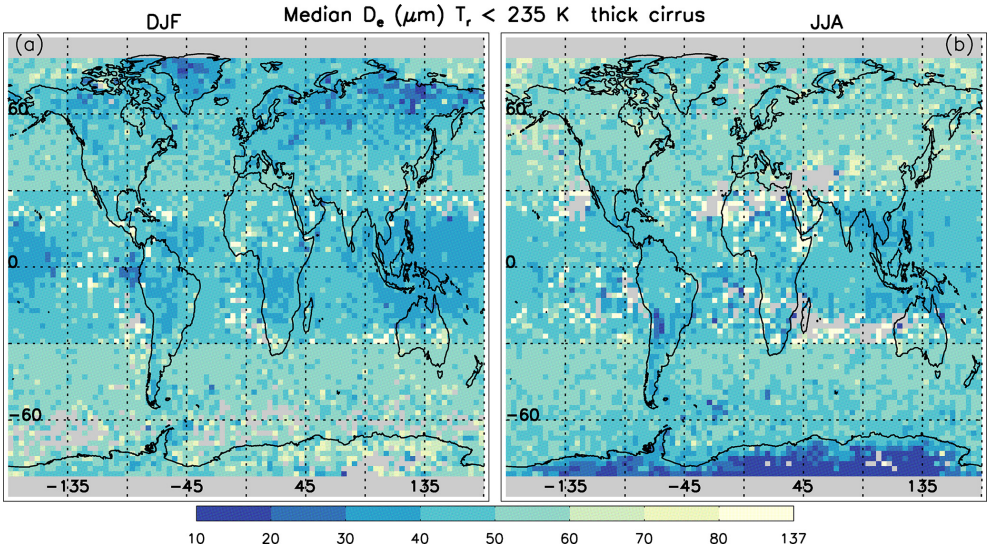

Figure 3. Global-seasonal maps of the median effective diameter D_e for thick cirrus($\sim 0.3 < \tau < \sim 3$) that include both WBC and in situ cirrus clouds. The color legend gives D_e in micrometers. Otherwise, as in Fig. 2.

sonable agreement with corresponding values in the cirrus cloud property climatology of Krämer et al. (2020) which is based on many field campaigns throughout the world. However, when the CALIPSO retrievals were restricted to thick clouds, the agreement degraded for N_i and IWC. Again, this raised the question of whether cirrus clouds having τ smaller and larger than 0.3 tend to be characterized by different physical properties and processes.

Figures 6 provides a means of investigating this question, evaluating N_i, IWC, D_e and the sampling densities for optically thin ($\sim 0.01 < \tau < \sim 0.3$) and thick ($\sim 0.3 < \tau < \sim 3$) cirrus clouds. Only retrievals over ocean are considered since variable land emissivities preclude retrievals over land for the thin clouds. These quantities are plotted in T_r vs. T_r–T_{top} space where T_{top} is temperature at cloud top and T_r is most of the time near mid-cloud (M2025). Thus, T_r–T_{top} is an index for cloud geometrical thickness. Figure 6a shows that for thick cirrus, the highest N_i (resulting from hom due to its magnitude) is found in relatively geometrically thin clouds (consistent with Fig. 10 in M2018), while Fig. 6d for optically thin cirrus is almost featureless with $N_i < 100\,L^{-1}$

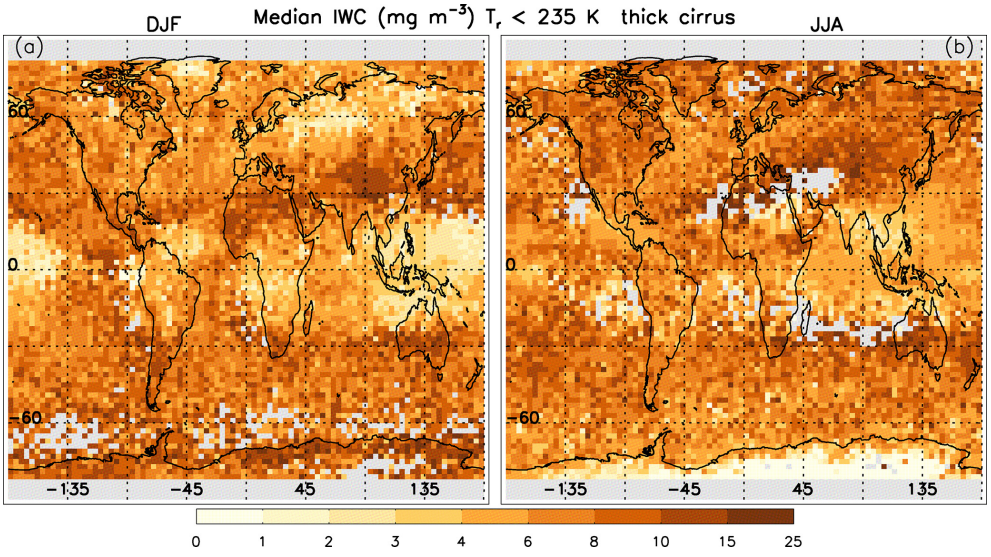

Figure 4. Global-seasonal maps of the median ice water content IWC for thick cirrus ($\sim 0.3 < \tau < \sim 3$) that include both WBC and in situ cirrus clouds. The color legend gives IWC in mg m^{-3}. Otherwise, as in Fig. 2.

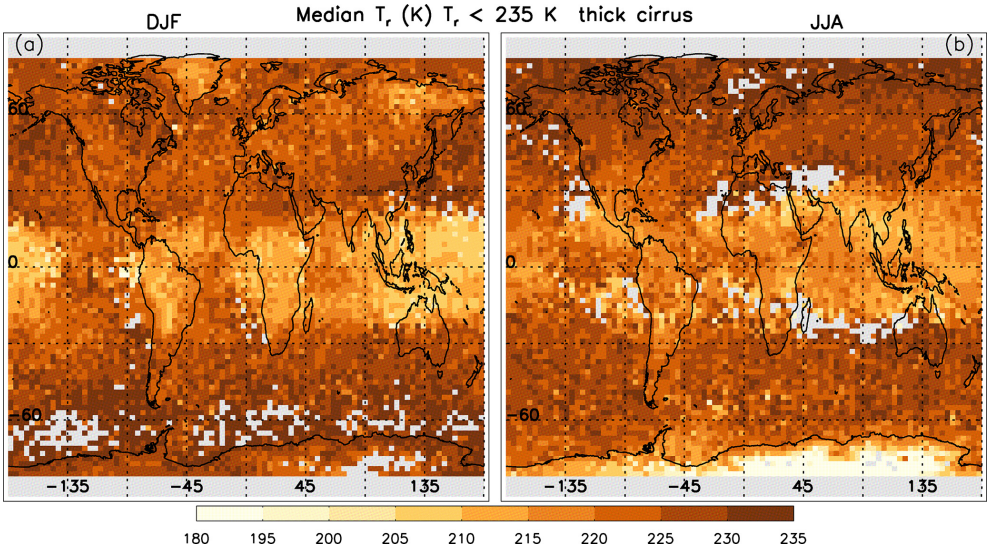

Figure 5. Global-seasonal maps of the median cirrus cloud radiative temperature T_r (K) for thick cirrus ($\sim 0.3 < \tau < \sim 3$) that include both WBC and in situ cirrus clouds. Otherwise, as in Fig. 2.

in general. Note that the retrievals characterize cloud layers (i.e., no vertical profiling within a cloud is possible).

The cirrus cloud remote sensing results from Dekoutsidis et al. (2023) and the cirrus cloud modeling results of Spichtinger and Gierens (2009a, b) both show that hom is primarily active only near cloud top, with the later showing relatively low N_i in the mid- to lower cloud where sedimenting ice crystals quench hom by lowering the RH_i. Based on this, geometrically thicker cirrus should have vertically averaged N_i much lower than N_i in the upper cloud and in geometrically thinner cirrus (assuming comparable thicknesses for the ice generating regions). These findings are consistent with our results for optically thick cirrus. IWC for these cirrus (Fig. 6b) is higher than for optically thin cirrus (Fig. 6e) clouds which exhibit much lower values, typically smaller than 4 mg m^{-3}. Jensen et al. (2024) show that N_i and IWC are higher in younger tropical cirrus clouds due to mesoscale temperature fluctuations from gravity waves that act to decrease them over time. This may help explain these results if hom cirrus are associated with young cirrus. Differences in D_e between the two τ categories are considerably less, as shown in Fig. 6c and f. For a given T_r, D_e tends to be quasi-constant, although decreasing for the geometrically thinnest clouds in both τ categories. To summarize, these results show

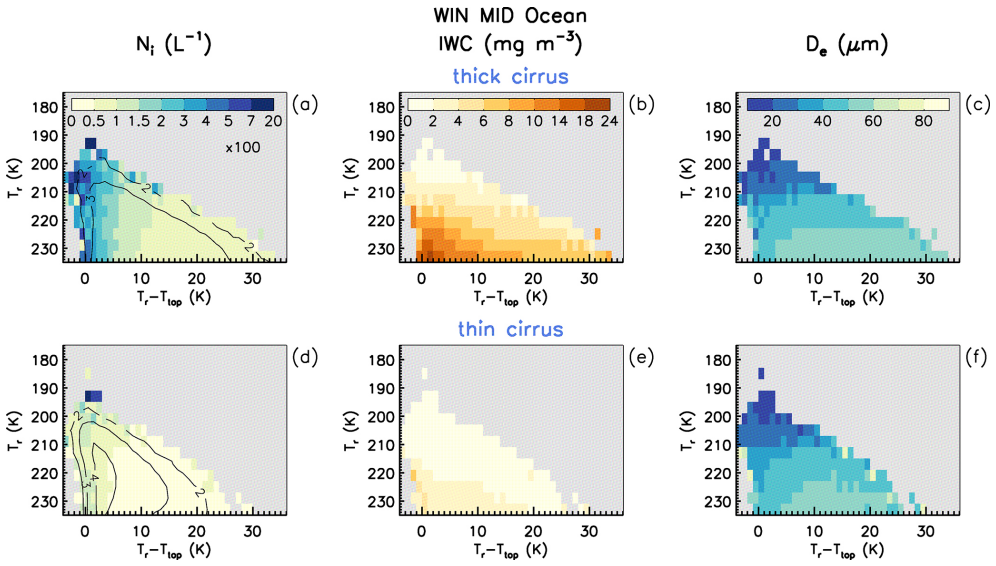

Figure 6. Cirrus cloud median ice particle number concentration N_i **(a, c)**, IWC **(b, d)**, and D_e **(c, f)** plotted in T_r vs. T_r–T_{top} space (for both WBC and in situ cirrus clouds) where T_{top} is cloud top temperature and T_r–T_{top} is related to cloud geometrical thickness. Panels **(a)**–**(c)** feature thick cirrus ($\sim 0.3 < \tau < \sim 3$) while panels **(d)**–**(f)** feature thin cirrus ($\sim 0.01 < \tau < \sim 0.3$). While only winter midlatitudes (WIN MID) over oceans are shown here during 2008, 2010, 2012, and 2013, these results were found to be valid at all latitudes and seasons over oceans. For panels **(a)** and **(d)**, the numbers in the color legend are to be multiplied by 100 to give N_i in L^{-1}.

that hom is active in optically thick cirrus (due to the high N_i in geometrically thin cirrus) but not in optically thin cirrus. Moreover, they show that hom mostly affects N_i and IWC, with perhaps a secondary impact on decreasing D_e (referring to Figs. 2, 3, S5 and S6 as well as Fig. 6). This suggests that the ratio IWC / D_e and therefore the extinction coefficient ($\alpha_{ext} = 3\,\text{IWC} / (\rho_i D_e)$, where ρ_i = bulk density of ice = 0.917 g cm^{-3}) may be sensitive to hom.

3.2 Using the extinction coefficient to identify hom-affected and het cirrus clouds

As described in M2018 and M2025, one of the cloud properties retrieved by this method is the cloud extinction coefficient for visible light, α_{ext}. Here we use this retrieved α_{ext} as a means for measuring the activity of hom since it contains the ratio IWC / D_e, which was shown in Sect. 3.1 to be sensitive to hom activity. For a given T_r, relatively high values of α_{ext} should correspond to a substantial impact from hom on the cloud microphysics.

To test this idea, N_i is plotted in T_r vs. log(α_{ext}) space in Fig. 7 for retrievals over ocean using all IIR samples, with τ ranging from ~ 0.01 to ~ 3, for the tropics, midlatitudes and high latitudes during winter (for both hemispheres) for in situ cirrus and WBC clouds. Light gray regions in these plots are where the number of samples is smaller than 10. Characteristic in all plots is a broad region on the left-hand side (relatively low α_{ext}) where $N_i < 30\,L^{-1}$. Although hom can produce such low concentrations at warmer temperatures and low updrafts (Krämer et al., 2016), hom tends to produce much higher N_i (Barahona and Nenes, 2009). To the right of this region is a gradient of increasing N_i, culminating in values of $N_i > 1000\,L^{-1}$. This gradient region is probably produced by varying degrees of hom activity, although het may also contribute to this gradient under conditions of relatively high INP concentration. It is evident that hom-affected cirrus clouds are common in both in situ cirrus and WBC. For WBC, hom appears quite active even at the highest temperatures. This can be understood if the cloud is glaciated by het freezing at $T > 235$ K and ice supersaturation s_i is already near the hom threshold. Then some cloud parcels are transported upwards across the 235 K isotherm, increasing s_i, with haze solution droplets freezing as they cross this isotherm. The main difference between these cloud types is in the tropics where in situ cirrus often appear to the right-hand side of the region predicted for pure hom (i.e., the triangles or squares), which will be discussed below. This may be due to deep convection overshooting the temperature level predicted for hom to activate, depositing ice mass at lower temperatures where in situ cirrus may subsequently form. Results like Fig. 7 are shown in Fig. S7 for land where this "overshooting effect" is more evident for in situ cirrus outside the tropics, perhaps due to stronger orography-induced updrafts over land. Also to be noted in Fig. S7 is the strong contribution from polar stratospheric clouds over Antarctica at very cold temperatures. To the right of this N_i gradient in Fig. 7, the boundary between peak N_i values and the "no data" region has a curious diagonal orientation (as well as the gradient) that may be explained from first principles.

To explore this further, two formulations of the Clausius–Clapeyron equation and the supersaturation threshold equation for hom, first derived in Lamb and Verlinde (2011), were used:

$$e_{si} = e_{s0} \exp\left[\frac{L_s}{R_g}\left(\frac{1}{T_0} - \frac{1}{T}\right)\right], \quad (1)$$

where e_{si} is water vapor pressure at ice saturation, L_s is latent heat of sublimation, R_g is the gas constant, T is temperature and e_{s0} and T_0 refer to water vapor pressure and temperature at the ice-point of water (6.11 hPa and 273.15 K, respectively). Reformulating Eq. (1) as described in Sect. 3.3.1 of Lamb and Verlinde (2011) gives an expression useful in calculating the supersaturation required for homogeneous ice nucleation:

$$e_s / e_{si} = \exp\left[\frac{L_f}{R_g}\left(\frac{1}{T} - \frac{1}{T_0}\right)\right], \quad (2)$$

where e_s = water vapor pressure at water saturation and L_f = latent heat of fusion. Finally, the threshold supersaturation ratio where hom occurs, S_i^f, was developed in Lamb and Verlinde (2011) from results in Koop et al. (2000):

$$S_i^f = 1.0 + 0.305 \frac{e_s}{e_{si}}. \quad (3)$$

Noting that the water vapor pressure at S_i^f, e_{hom}, is simply $e_{hom} = S_i^f e_{si}$, water vapor densities are obtained from the gas law ($\rho_{hom} = e_{hom}/(R_v T)$ and $\rho_{si} = e_{si}/(R_v T)$, R_v = gas constant for water vapor) to predict the maximum IWC resulting from hom:

$$IWC_{hom} = \rho_{hom} - \rho_{si}. \quad (4)$$

But to relate $IWC_{hom}(T)$ to retrieved IWC in T_r vs. α_{ext} space, a corresponding α_{ext} is needed which requires D_e. For the tropics, the PSD mean ice particle maximum dimension D_{mean} was related to T using the CEPEX PSD scheme described in Mitchell et al. (1999), where only the large ice particle mode was used. For outside the tropics, a D_{mean}–T relationship based on the SPARTICUS field campaign (Mishra et al., 2014) was used, which is $\log(D_{mean}) = 0.0307\,T + 3.169$, with D_{mean} in micrometers and T in °C. Using the ice particle mass- and projected-area-dimensional relationships from Erfani and Mitchell (2016) and an exponential gamma PSD, D_e was calculated from D_{mean} as described in that study. This gives D_e under "normal" conditions. To estimate D_e under maximum hom conditions (corresponding to Eq. 4), we use panels (h), (i) and (l) of Fig. 10 over land for high latitudes and for midlatitudes during winter which show that when hom is most active, D_e decreases from "normal values" of ∼ 55 to ∼ 35.5 µm for T between 219 and 235 K, or by a factor of 0.646. Thus, we apply this factor to D_e estimated from D_{mean} to estimate D_e for maximum hom conditions. Finally, we calculate N_i by converting this D_e back to D_{mean} for an exponential PSD using Eq. (7) in Mitchell et al. (2020) and then calculating the PSD slope parameter λ from D_{mean} ($\lambda = 1/D_{mean}$). For the region where hom is most active, N_i is N_{max} calculated as

$$N_{max} = \frac{\Gamma(\nu+1)\,IWC_{hom}\lambda^{\beta}}{\alpha\,\Gamma(\beta+\nu+1)}, \quad (5)$$

where ν is a parameter in the gamma PSD $N(D) = N_0 D^{\nu} \exp(-\lambda D)$ and α and β define the ice particle mass relationship $m = \alpha D^{\beta}$, where $\nu = 0$ here. The values of α and β were obtained from Erfani and Mitchell (2016) in the same way that D_e was calculated; N_{max} predicted from Eqs. (5) and (1) of Schneider et al. (2021) is overplotted in Fig. 7 as shown by the triangles and squares, respectively, with the color inside the triangles/squares indicating the concentration range (based on the color bar). Schneider et al. (2021) provide an empirical expression for S_i^f based on experiments in the AIDA cloud chamber.

Figure 8a to c show the retrieved median IWC plotted in T_r vs. $\log(\alpha_{ext})$ space for all samples over oceans (both in situ and WBC), with triangles predicted from Eq. (4) overlaying these retrieved IWCs. The different D_{mean}–T relationships for the tropics and for outside the tropics yield slightly different $\alpha_{ext}(T)$ associated to $IWC_{hom}(T)$ (since $\alpha_{ext} = 3\,IWC\,/\,(\rho_i D_e)$). The color within the triangle indicates the approximate IWC_{hom} value via the color bar legend. It is seen that the color within the triangles matches the background color in almost all cases, showing good agreement between basic theory and the retrieved IWC where hom is expected to be most active. IWC_{hom} was also calculated from Eq. (1) in Schneider et al. (2021), shown by the squares in Fig. 8. There is close agreement between the theoretical (i.e., Eq. 3) and experimental methods, where both methods address the homogeneous freezing of solution haze droplets based on the activity of water in a solution droplet (Koop et al., 2000) and do not address the homogeneous freezing of activated cloud droplets. In panels (d) to (f), retrieved median D_e is plotted in T_r vs. $\log(\alpha_{ext})$ space for all samples over oceans, with theoretical and experimental hom D_e indicated by the triangles and squares, respectively, with their color based on the same color legend as used for the retrievals. The predicted and retrieved D_e values are in general agreement for this hom-active region. Results like Fig. 8 but over land are shown in Fig. S8.

There is a close correspondence between the predicted triangle (or square) color and adjacent retrieval colors in Figs. 8 and S8, indicating reasonably good agreement between theory and observations. The predicted triangles and squares in Figs. 7 and S7 show the maximum N_i expected for a given T_r (thus indicating the region of maximum hom activity). The predicted colors (triangles and squares) tend to indicate higher N_i than the adjacent background retrieved N_i colors, which is consistent with expectations that hom events are diluted through mixing and entrainment (Jensen et al., 2012). The diagonal orientation of this hom region is a consequence of the Clausius–Clapeyron equation that predicts lower satu-

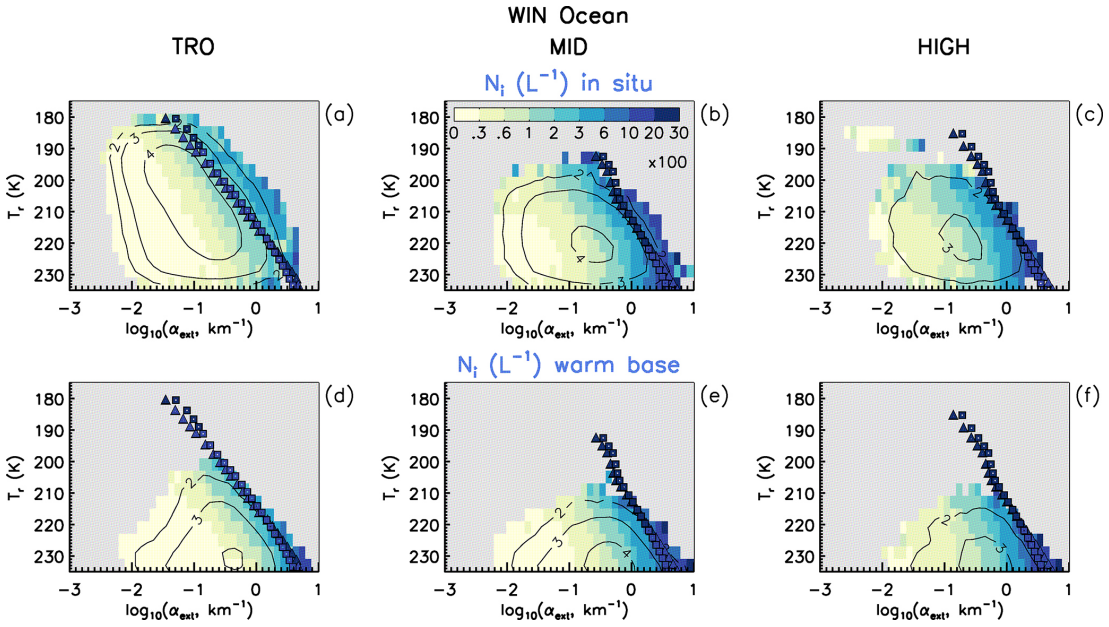

Figure 7. Median retrieved ice particle number concentration N_i plotted in T_r vs. $\log(\alpha_{ext})$ space to separate the het- and hom-regimes. The black contours show the $\log_{10}$ of the number of samples. The numbers in the color legend are to be multiplied by 100 to give N_i in L^{-1}. Retrievals are over ocean using all IIR samples for in situ cirrus and WBC as indicated, with τ ranging from ~ 0.01 to ~ 3, for the tropics (TRO, panels **a** and **d**), midlatitudes (MID, panels **b** and **e**), and high latitudes (HIGH, panels **c** and **f**) during winter (WIN) using both hemispheres during 2008, 2010, 2012 and 2013. The triangles and squares represent theoretical and empirical predictions for ice nucleation through hom. The color within each triangle or square indicates the approximate N_{max} for pure hom conditions via the color bar legends.

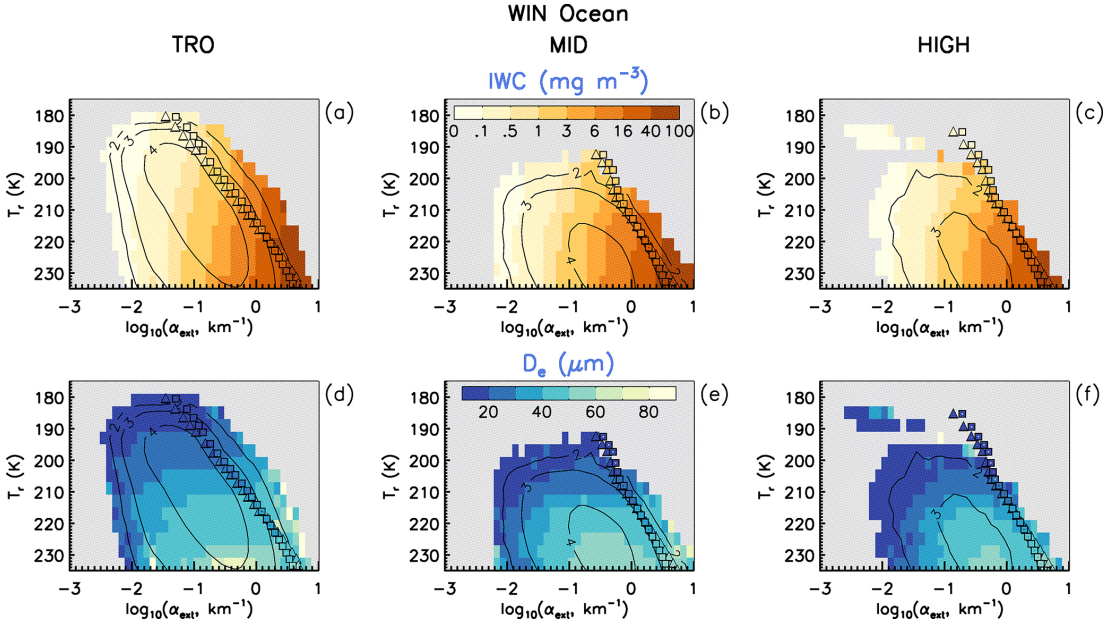

Figure 8. Median retrieved IWC **(a–c)** and D_e **(d–f)** plotted in T_r vs. $\log(\alpha_{ext})$ space to separate the het- and hom-regimes. The black contours show $\log_{10}$(number of samples). The color-bars give IWC (mg m^{-3}) and D_e (μm). Retrievals are over oceans using all IIR samples (both in situ and WBC), with τ ranging from ~ 0.01 to ~ 3, for the tropics (TRO, panels **a**, **d**), midlatitudes (MID, panels **b**, **e**), and high latitudes (HIGH, panels **c**, **f**) during winter (WIN) using both hemispheres during 2008, 2010, 2012 and 2013. The triangles and the squares represent predictions from simple hom theory using Eq. (4) and Schneider et al. (2021), respectively, and the color within each triangle or square indicates the approximate IWC_{hom} **(a–c)** and hom D_e **(d–f)** values via the color bar legends.

ration water vapor pressure and density as T decreases. In the tropics, the predicted colors indicate considerably higher N_i values than the adjacent retrieval values. This may indicate that hom is less active in the tropics for our cloud sampling.

The black contours in Figs. 7, S7, 8 and S8 show the pixel count densities in T_r vs. $\log(\alpha_{ext})$ space. Outside the tropics, the triangles/squares coincide with relatively low pixel counts, indicating the frequency of occurrence for hom events is quite low, consistent with theoretical expectations (e.g., Krämer et al., 2016).

3.3 Microphysical attributes of het and hom-affected cirrus clouds

It has now been shown that α_{ext} seems to be a suitable metric to identify varying degrees of hom activity, but how can this be used to quantify the contribution of hom-affected cirrus clouds in terms of frequency of occurrence and radiative impact? To address this question, a method is presented that estimates the fraction of hom-affected cirrus clouds such that these clouds are strongly altered microphysically relative to cirrus associated with relatively low N_i, such as cirrus formed through het and aged, dissipating/sublimating cirrus clouds (formed either through hom or het). Henceforth the former will be referred to as hom cirrus and the latter as het cirrus. These dissipating cirrus clouds are microphysically described in Fig. 6 of Krämer et al. (2020) where $RH_i < 100\,\%$. These two categories will now be described and finally quantified.

The median N_i and median D_e corresponding to various temperature intervals in Figs. 7 and 8 were plotted against α_{ext} in Fig. 9 (panels a–f and g–l, respectively) for both winter and summer. These retrievals are over oceans for only in situ cirrus clouds, and a similar plot, Fig. S9, is given for WBC clouds. When median D_e was set equal to the sensitivity limit (M2025), it was not plotted, which rarely occurred. Colors indicate the 4 K temperature interval corresponding to the retrievals. Outside the tropics, it is seen that two populations exist, characterized by different $d\log(N_i)/d\log(\alpha_{ext})$ slopes in the case of N_i or trends in the case of D_e, mostly for the higher temperatures. If one were to describe the "warm-colored" ($T > 215$ K) N_i data with two linear fits, a change in slope occurs around $\alpha_{ext} \approx 0.3\,km^{-1}$. The increased slope for $\alpha_{ext} > 0.3\,km^{-1}$ is where median D_e increases slowly or starts decreasing. For $T_r < 215$ K, these trends are less coherent. This behavior suggests a transition from het cirrus to hom cirrus. For N_i in the tropics, there is no apparent change in slope, which may indicate that hom is less active in the tropics. Note that this analysis is based on clouds having $\tau < \sim 3$ and thus does not consider thick cirrus clouds originating from deep convection where $\tau > 3$ and hom is probably active in the strong updrafts. Note that these observations apply to both in situ and WBC clouds, suggesting that similar physics applies to both cloud types.

A maximum in D_e is expected to occur after a slope change regarding N_i due to the competition for water vapor among a relatively high concentration of newly formed ice crystals. This competition reduces the growth rates of these ice crystals, keeping them relatively small. Other than hom, we know of no process that can explain the decrease in D_e at higher extinction shown in Fig. 9. Since for spherical ice the spherical volume radius R_v is proportional to $(1/N_i)^{1/3}$, it is apparent that even for non-spherical ice crystals, it will take a larger change in N_i to affect a significant change in R_v or D_e through vapor competition effects. Thus, regarding D_e and N_i, a decrease in D_e caused by hom would be a more conservative criterion for defining hom cirrus. This would be more pragmatic if one were primarily interested in the impact of hom on radiation since cloud radiative properties are parameterized in terms of D_e and IWC (e.g., Gettelman et al., 2010; Emde et al., 2016). For this reason, we define hom cirrus as cirrus having an extinction exceeding that at the D_e maximum.

3.3.1 Hom intensity

To better understand these principles, these ideas can be tested in an environment where INP concentrations are higher, that is, over land. Figure 10 is like Fig. 9 except the retrievals are over land and therefore only for optically thick in situ cirrus ($\tau > \sim 0.3$). Despite the different ranges of optical depth in Figs. 9 and 10, observations are qualitatively similar. Regarding the N_i plots (panels a–f) in Fig. 10, there is a clear inflection point around $\alpha_{ext} = 0.2$ to $0.3\,km^{-1}$ where the N_i slope changes for $215 < T_r < 235$ K in all latitude bands and around $\alpha_{ext} = 0.1$ to $0.2\,km^{-1}$ for $T_r < 215$ K in three latitude bands. Note that consistent changes of slope or trend of opposite sign are seen in the D_e plots (panels g–l). Referring to Fig. 7, this change in N_i slope is due to hom with hom affecting the cirrus microphysics for $\alpha_{ext} \geq 0.3\,km^{-1}$. The slope of the N_i data for 235–215 K for $\alpha_{ext} \geq 0.5\,km^{-1}$ appears related to the production rate of ice crystals through hom (i.e., N_i is higher for steeper slopes) and as such can be viewed as a measure of the intensity of hom. The midlatitude slope over land is greater during winter relative to summer, consistent with N_i in Figs. 2 and S5. This may be due to higher cirrus cloud updrafts over land, especially over mountainous terrain. For $\alpha_{ext} < 0.3\,km^{-1}$, het is expected to dominate, and the N_i distributions are almost flat outside the tropics, with N_i increasing somewhat for decreasing α_{ext} in the tropics. Figure S10 provides similar results for WBC clouds.

3.3.2 A cirrus cloud Twomey effect?

Most evident when comparing Figs. 9 and 10 (or Figs. S9 and S10) for $\alpha_{ext} < 0.3\,km^{-1}$ (i.e., the het cirrus regime) is that median N_i is higher over land (up to a factor of 10), presumably due to higher INP concentrations over land. For direct comparison with Fig. 10, results similar to Fig. 9 but

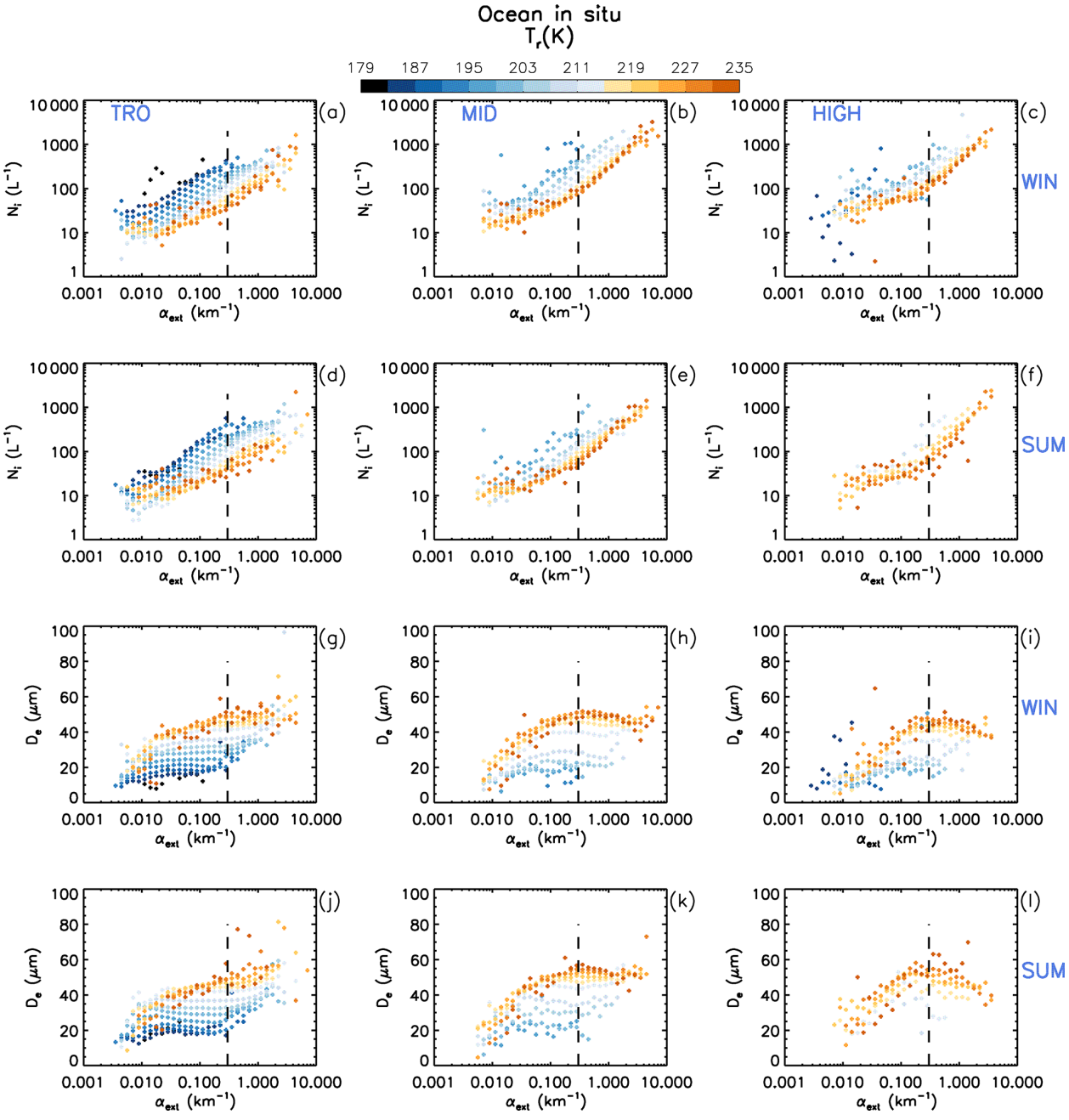

Figure 9. The dependence of median log N_i (upper half, panels **a–f**) and median D_e (lower half, panels **g–l**) on α_{ext} for all in situ cirrus samples over oceans ($\sim 0.01 < \tau < \sim 3$). The various T_r intervals (4 K per interval) are given by the color legend. Each row features the tropics (TRO), midlatitudes (MID), and high latitudes (HIGH) in both hemispheres for either winter (WIN) or summer (SUM). The vertical dashed line at $\alpha_{ext} = 0.3\,km^{-1}$ in panels **(a)–(f)** marks where a change in slope generally occurs for the 231–235 K interval. These same dashed line positions are also indicated in panels **(g)–(l)** showing their relation to the D_e maximum.

for thick cirrus (like Fig. 10) are shown in Fig. S11. In the lower half of Figs. S11 and 10, D_e is related to α_{ext} where it is evident that D_e is substantially smaller over land relative to oceans for $\alpha_{ext} < 0.3\,km^{-1}$. Since N_i is higher over land (although perhaps not at high latitudes, based on Fig. S11), this suggests that higher INP concentrations over land may be producing a "Twomey effect" in het cirrus clouds over land. While higher updrafts over land could also enhance INP and N_i concentrations, note that updraft effects are implicit in Figs. 9, S11 and 10. That is, higher updrafts are associated with higher IWC (Hu et al., 2021; Mitchell, 1988) and higher extinction is associated with higher IWCs. The appar-

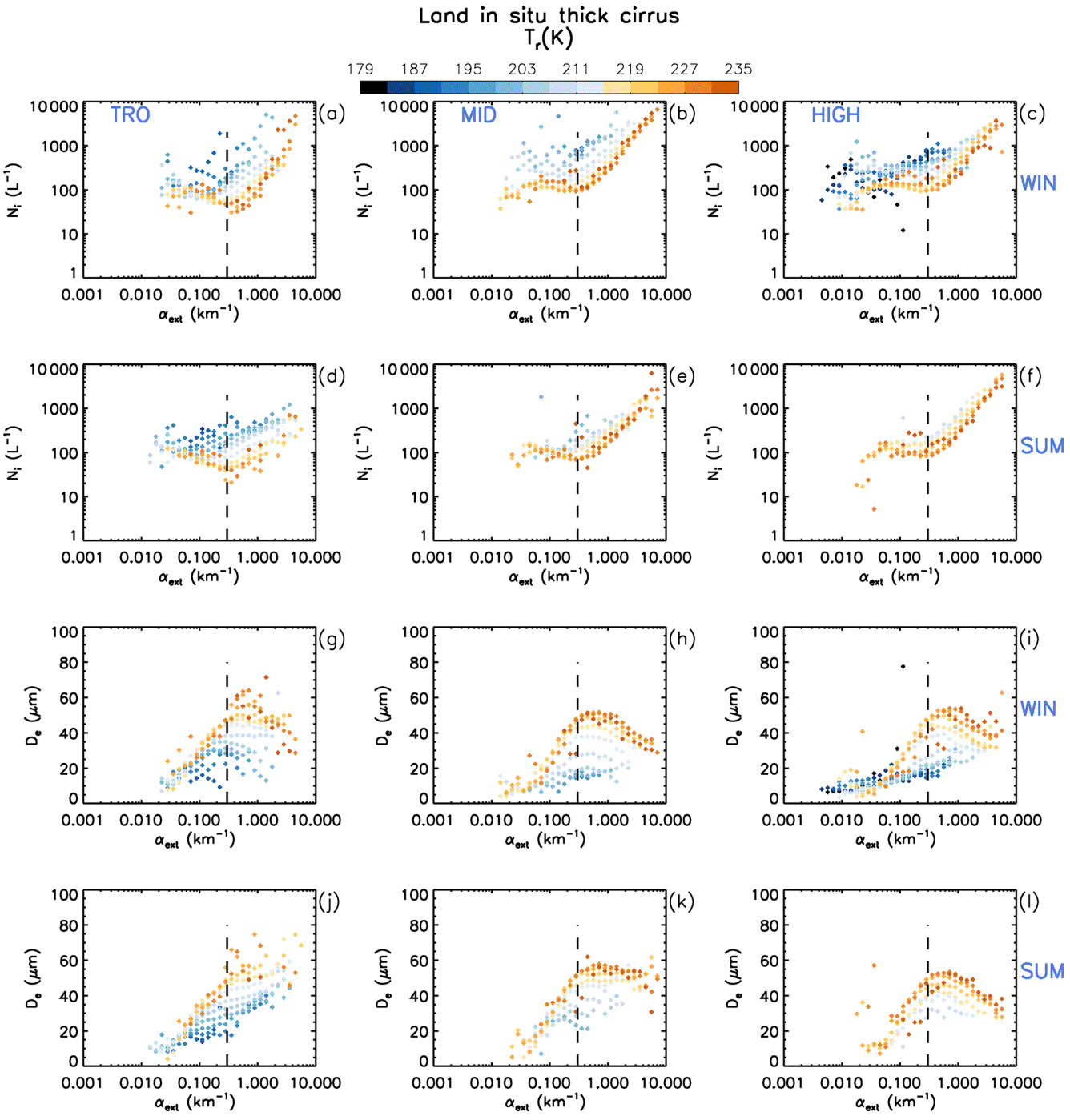

Figure 10. Same as in Fig. 9 but for retrievals over land for optically thick in situ cirrus ($\sim 0.3 < \tau < \sim 3$).

ent Twomey effect here is associated with $\alpha_{ext} < 0.3\,km^{-1}$ where updrafts are expected to be relatively weak over both ocean and land.

3.4 Quantifying the contribution of hom-affected cirrus clouds based on extinction and D_e

As shown in Figs. 9 and 10, D_e exhibits a maximum where $d(D_e)/d(\log(\alpha_{ext})) \approx 0$. This maximum generally occurs for $\alpha_{ext} > 0.3\,km^{-1}$ and serves as a more conservative estimate of the transition from het to hom-affected conditions. Figure 11 shows plots of N_i in T_r vs. $\log(\alpha_{ext})$ space for the

tropics, midlatitudes and high latitudes over oceans for DJF and JJA in each hemisphere, where $\sim 0.01 < \tau < \sim 3$. The transition from het to hom cirrus at each T_r value is where D_e is maximum, and this maximum is marked by the black "+" signs. However, in the tropics and in the summer NH midlatitudes, D_e maxima were ambiguous and the transition from het to hom cirrus at a given T_r was determined by a N_i threshold, N_{thres}. This threshold is the mean value of N_i that correspond to all the D_e maxima (51 in total) in the extra-tropics. The value and standard deviation of N_{thres} is $118 \pm 57\,L^{-1}$ where the standard deviation is probably subject to variations in INP concentration (Haag et al., 2003). The hom threshold was assigned to the α_{ext} having the corresponding N_i closest to N_{thres}. In two extra-tropical datasets (DJF MID SH and DJF MID NH), N_{thres} was also used to estimate the hom threshold for $T_r < 219\,K$ and $T_r < 207\,K$, respectively.

The horizontal dashed line in Fig. 11 indicates the temperature T_{min}, below which the number of cirrus cloud samples was too low for statistically meaningful analysis. The region of hom-affected cirrus clouds is thus defined as the region bounded by the + signs in the vertical and the dashed line in the horizontal, with the right-hand vertical boundary defined by the absence of data and the lower horizontal boundary defined by the 235 K isotherm. Also plotted in Fig. 11 are alternating solid and dashed curves indicating the fraction of samples, in increments of 0.10 from right to left, having a larger extinction than the extinction corresponding to the curve (at a given T_r). This provides estimates of the fraction of hom cirrus for a given T_r. For reference, the triangles predicted from hom theory are also shown (same as in Fig. 7). Overall, α_{ext} at het–hom transitions is found between $\sim 1.8\,km^{-1}$ (in the tropics) and $0.02\,km^{-1}$ (in the winter Arctic) and tends to decrease as T_r decreases (similar to the temperature dependence of N_i predicted from hom theory). Similar results were found for cirrus clouds over land ($\sim 0.3 < \tau < \sim 3$), which are shown in Fig. S12.

These hom region boundaries were incorporated into look-up-tables that relate 4 K temperature intervals to latitude band, season and surface type (oceans or land) for determining whether a sample was het cirrus or hom cirrus. When $D_e >$ sensitivity limit, we set the sample as het cirrus. Applying this D_e sensitivity limit to all cirrus cloud samples over oceans reduces the estimated hom fraction by less than 8 % at $T_r < 211\,K$. The largest changes are for T_r within the 223–235 K interval, where the hom fraction is reduced by 50 % in the tropics, and by 22 %–25 % in the extra-tropics.

3.4.1 Results

Results from this analysis over oceans ($\sim 0.01 < \tau < \sim 3$) are shown in Figs. 12 and 13, where the hom fraction vs. T_r is shown in red. The hom fraction, which is defined as the number of hom cirrus pixels divided by the total number of cirrus pixels, varies with T_r and is typically smaller than 0.4 (with five exceptions at the lowest T_r outside the tropics). WBC clouds, which tend to have stronger updrafts than in situ cirrus (Wernli et al., 2016), contribute primarily to the hom fraction at higher T_r as shown in Appendix A. In addition, Fig. 12 shows median N_i vs. T_r for all cirrus (blue), for het cirrus (black), and for hom cirrus (orange). The "all cirrus" and "het cirrus" profiles are identical where the hom fraction is null and they are close when the hom fraction is relatively small. Conversely, when the hom fraction is relatively large, the "all cirrus" and "hom cirrus" profiles become closer. For the latter, median N_i is most of the time larger than $200\,L^{-1}$. In this way, Fig. 12 shows how the T_r dependence of the hom fraction affects median N_i.

Hom may occur through (1) the freezing of haze solution droplets (Koop et al., 2000) and (2) the freezing of supercooled cloud droplets advected across the isotherm $\sim 235\,K$ (e.g., Rosenfeld and Woodley, 2000). If (1) and (2) are comparable in their frequency of occurrence, an abrupt increase in median all cirrus N_i should be evident in Fig. 12 in the 231–235 K range (given typical non-convective cirrus updrafts of 10 to $30\,cm\,s^{-1}$). Since such an abrupt increase is not evident in Fig. 12, it appears that (2) does not contribute significantly to N_i, even in the tropics. This is consistent with Avery et al. (2020), Costa et al. (2017), and Mitchell and d'Entremont (2012) where it was shown that liquid water is rare in clouds over the range 239–235 K. This applies to both in situ cirrus and WBC clouds and is consistent with the definition of LOC in Luebke et al. (2016) where it is stated that LOC are restricted to pure ice clouds having $T < 250\,K$ (−23 °C). When considering only hom cirrus N_i, an increase in hom N_i with T_r is seen in the tropics for $T_r > 215\,K$, which might be attributed to (2), but it applies to only 2 % of the sampled cirrus at 231–235 K, as shown by the hom fraction curve.

Figure 13 is similar to Fig. 12 except cloud optical depth τ is evaluated instead of N_i. Noting the log scaling of τ, it is clear that hom has a non-trivial impact on median τ. That is, aerosol-cloud-radiation interactions for cirrus clouds are probably greatest for optically thick cirrus where hom is active. The maximum CRE change is expected when INP concentrations are just enough to completely prevent hom but do not exceed this concentration by more than a factor of ~ 3 (Storelvmo et al., 2013). Under this condition, the blue median τ profile for all cirrus and the black het cirrus τ profile should be the same. Thus, the difference between the blue and black τ profiles reveals the potential relative CRE impact of INPs (e.g., Mitchell and Finnegan, 2009; Storelvmo et al., 2013; Gruber et al., 2019). Finally, it should be noted that the relatively low hom fractions in the tropics are believed to partly result from sampling restrictions, where only cirrus having $\tau < \sim 3$ are sampled. That is, hom is probably very active where deep convection occurs, but these clouds are characterized by $\tau \gg 3$.

Global geographical distributions of hom fractions in the atmospheric column are shown for DJF and JJA in Fig. 14.

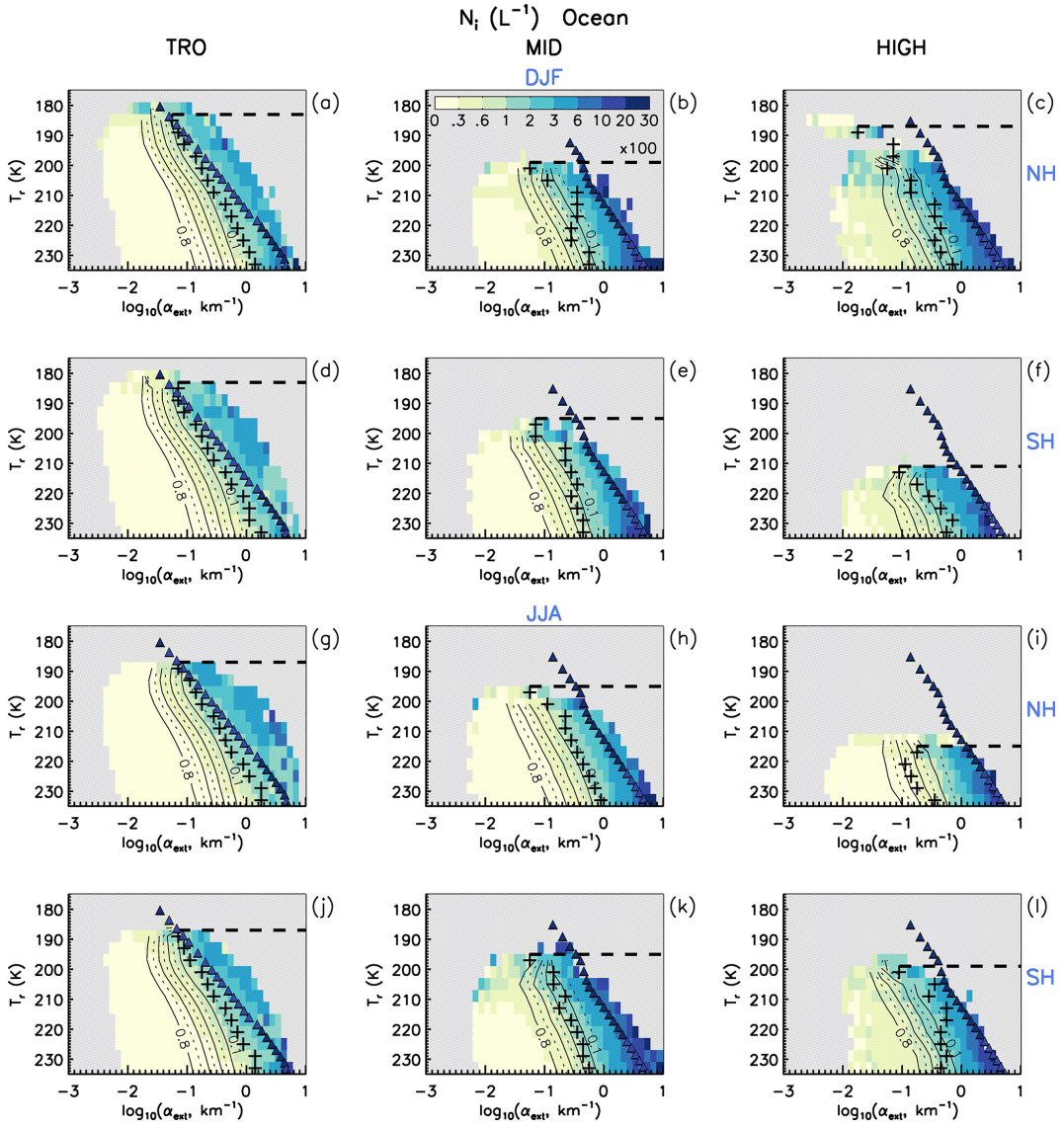

Figure 11. Procedure for identifying hom-affected cirrus over oceans using all samples ($\sim 0.01 < \tau < \sim 3$). The hom-affected region is bounded by the D_e maxima (+ signs) in the vertical and in the horizontal by the 235 K isotherm and T_{min} (dashed line) below which sampling is too low for meaningful analysis. Other features are as in Fig. 7. The alternating solid-dashed contour lines are varied with increments of 0.10 (i.e., 10 %) from right to left to show the approximate fraction of samples (at a given T_r) within the hom-affected region. Each row features the tropics (TRO), midlatitudes (MID), and high latitudes (HIGH) for either the northern (NH, panels **a–c** and **g–i**) or southern (SH, panels **d–f** and **j–l**) hemisphere in DJF and JJA during 2008, 2010, 2012, and 2013.

Because hom clouds tend to have an overall larger optical depth than het clouds, the hom fraction over land which is based on optically thick cirrus clouds is expected to be overestimated. Therefore, we applied a zonal correction factor at 2° resolution which was estimated from samples over oceans as

$$\text{Correction factor} = \frac{\text{fraction}_{\text{All}}}{\text{fraction}_{\text{thick}}}, \quad (6)$$

where $\text{fraction}_{\text{All}}$ is the hom fraction using all samples and $\text{fraction}_{\text{thick}}$ is the hom fraction using samples of optically thick cirrus clouds. This correction factor was multiplied by the hom fraction based on optically thick cirrus to produce the hom fractions shown in Fig. 14. For a given grid cell (i.e., column of atmosphere), the T_r-dependent hom fractions were weighted by the normalized fraction of samples at each level and vertically integrated to yield the mapped hom fraction. The hom fraction ranges between 0.02 in the tropics and 0.6 at high latitudes in the SH. Relatively few grid cells are light gray to indicate that fewer than 10 samples constitute that grid cell (see also Fig. A1a and b for cloud sampling). Since this methodology is based on T_r-dependent hom thresholds

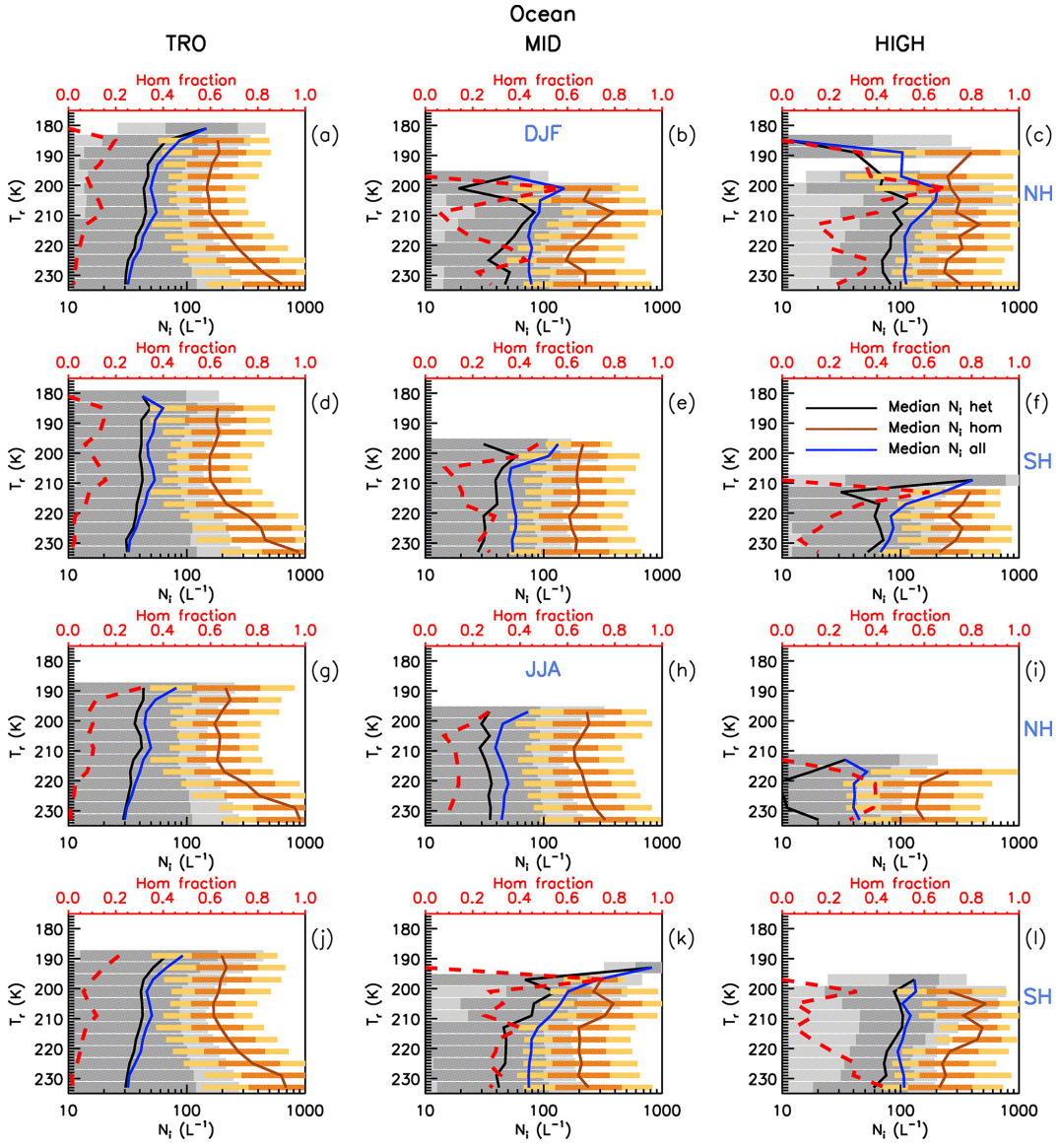

Figure 12. The T_r dependence of the hom fraction (red dashed) for all samples over oceans ($\sim 0.01 < \tau < \sim 3$). Each row features the tropics (TRO), midlatitudes (MID), and high latitudes (HIGH) for either the northern (NH) or southern (SH) hemisphere in DJF and JJA during 2008, 2010, 2012, and 2013. Also shown are median N_i profiles for all cirrus (blue), for het cirrus (black), and for hom cirrus (orange). The 25th to 75th percentile range is indicated by darker gray shading for het cirrus and darker orange shading for hom cirrus, while the 10th to 90th percentile range is indicated by lighter gray shading for het cirrus and lighter orange shading for hom cirrus.

determined for 30° latitude bands, discontinuities in the hom fraction are common between latitude bands. Thus, the hom fractions in Fig. 14 are qualitative, and there should actually be a more gradual transition between latitude bands where discontinuities occur.

A case in point is the discontinuity at 60° N in Fig. 14 for JJA, with relatively high hom fractions north of 60° N. As seen in Fig. 11i, the maximum D_e values at the four warmest temperature levels between 221 and 233 K occur at low α_{ext} relative to the other panels, corresponding N_i values are relatively small, and hom fractions in Figs. 12i and 13i range between 0.3 and 0.4. Because this was unexpected, we examine in Fig. 15 the dependence of N_i, D_e and IWC on extinction for the four seasons for the temperature bin at 229 K. Other temperature intervals (having a mid-temperature of 233, 225 and 221 K) exhibited the same behavior. Regardless of temperature, the maximum D_e value at low α_{ext} occurs only in JJA, and no marked difference between the three other seasons is observed. In addition, N_i is lowest in JJA (consistent with largest D_e in JJA), with a change in slope consistent with the D_e maximum, and IWC is consistent with the N_i–D_e behavior. A possible reason for this low het–hom

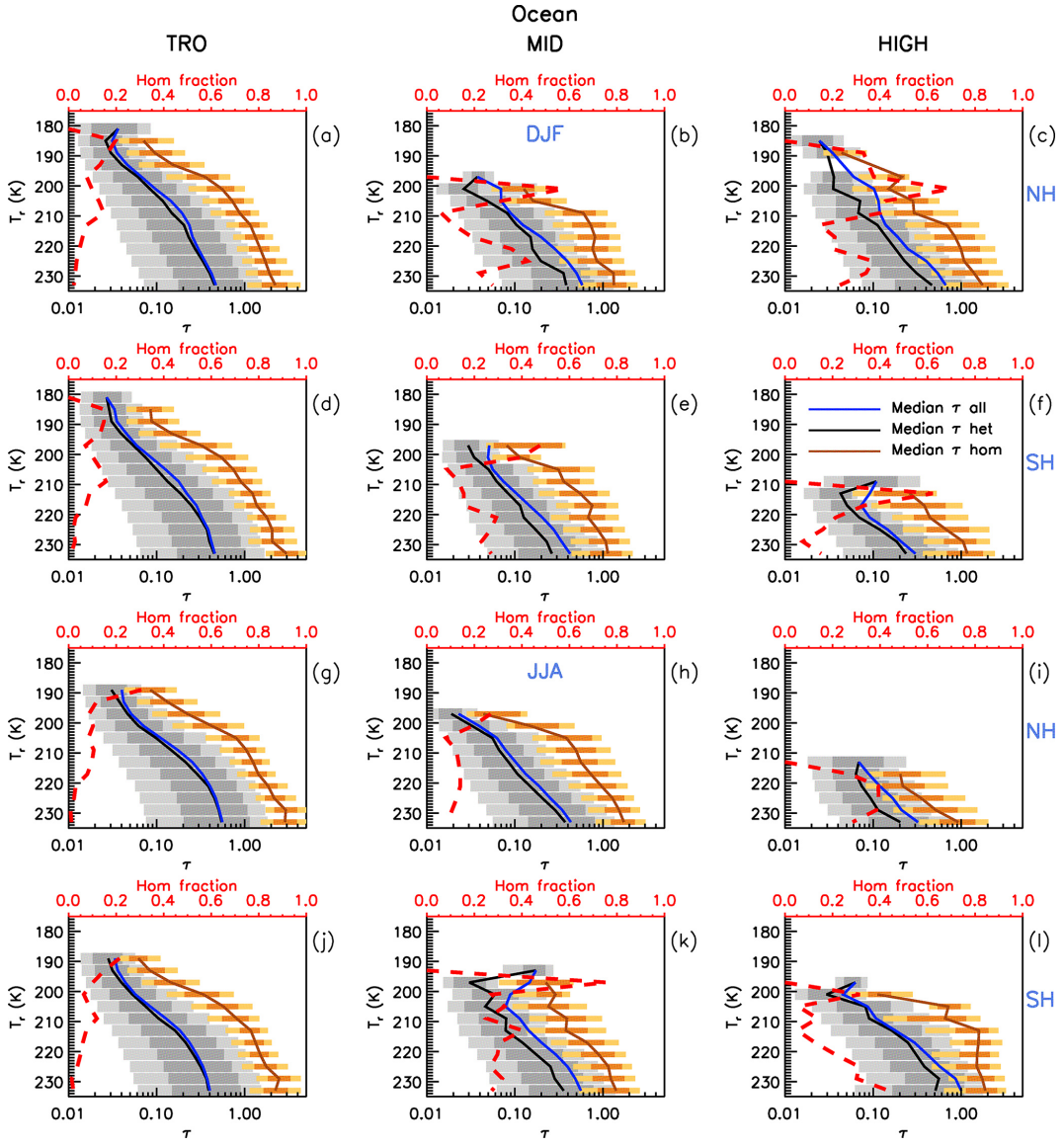

Figure 13. As in Fig. 12, but instead of showing median N_i profiles, median τ profiles are shown for all cirrus (blue), for het cirrus (black), and for hom cirrus (orange).

α_{ext} threshold and resulting high hom α_{ext} threshold and resulting high hom fraction during JJA is relatively low INP concentrations which would allow the RH_i in an ascending air parcel to reach the hom threshold more frequently due to lower water vapor removal rates by ice (Krämer et al., 2016). Evidence for lower INP concentrations can be found in the CALIOP dust aerosol optical depth (DAOD) climatology of Song et al. (2021, Fig. 6) where JJA has the lowest DAOD north of 60° N, but dust concentrations were not vertically resolved in this figure. Froyd et al. (2022) reported aircraft measured dust concentrations at cirrus levels using the Particle Analysis by Laser Mass Spectrometry (PALMS) instrument which discriminated between mineral dust and other aerosol types. Dust mass and number concentration were determined from simultaneous measurements by PALMS and of size-resolved aerosol number concentration. Such measurements were made during four global flights mostly over the Pacific and Atlantic Ocean, from the Arctic to Antarctica and back. Dust concentrations were lowest during August and October north of 60° N regarding the 4 months (also including February and May) of the ATOM field campaign. However, estimated dust mixing ratios in Kok et al. (2021) poleward of 60° N from 200–400 hPa show slightly higher values for JJA relative to DJF. Overall, if this interpretation is correct, it suggests that changes in relatively low levels of dust concentration can significantly affect the D_e of cirrus clouds and hence their optical properties.

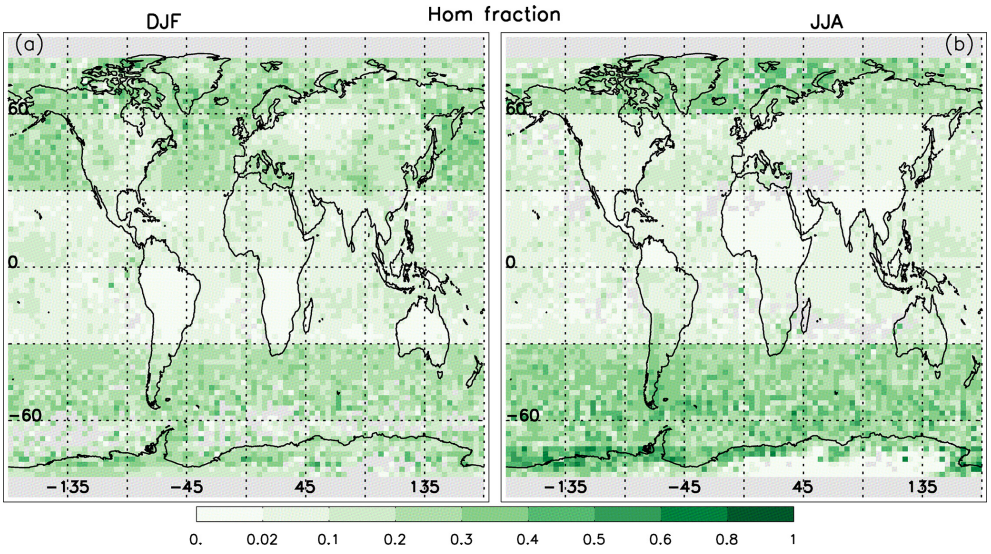

Figure 14. Geographical distribution of the fraction of cirrus clouds affected by hom during **(a)** DJF and **(b)** JJA where the color bar indicates the hom fraction. See text for details.

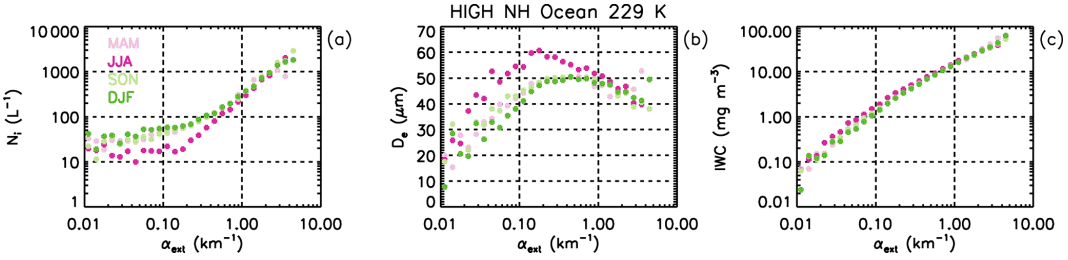

Figure 15. Seasonal analysis of the region 60–90° N over oceans for the 229 K temperature level in terms of the extinction dependence of **(a)** N_i, **(b)** D_e, and **(c)** IWC. Extinction at maximum D_e, indicative of het–hom transition, is the smallest in JJA (dark pink) compared to MAM (light pink), SON (light green) and DJF (dark green), yielding the greatest hom fraction during JJA.

Also of interest are the seasonal changes in hom fraction between 30 and 60° N in Fig. 14. Relative dust contributions of the world's main dust source regions are estimated in Kok et al. (2021) and Froyd et al. (2022), with dust from Asian deserts (e.g., Taklimakan and Gobi) more likely to reach cirrus cloud levels in the UT due to ascent within frontal systems, orographic uplift, and dry convection. Asian dust emissions to the UT were maximum in summer (JJA), contributing 59 %–73 % of dust to the NH UT, but with minimal contributions during winter (also see the Supplement of Kok et al., 2021). Regions downwind of these Asian dust sources in Fig. 14 (into North America) undergo a strong seasonal change regarding their hom fraction, being relatively high in winter and relatively low in summer. This may be due to the above noted changes in mineral dust, with higher UT dust concentrations promoting het cirrus clouds. This phenomenon is discussed in greater detail in Mitchell and Finnegan (2009), where a climate intervention method known as cirrus cloud thinning (CCT) was proposed. A similar phenomenon may be occurring in the SH over the Southern Ocean (30–60° S), where the main UT dust source is South America. Estimated dust concentrations between 200 and 400 hPa are highest during summer (DJF) and lowest during winter (Kok et al., 2021, the Supplement). In Fig. 14, hom fractions over the Southern Ocean tend to be lower in summer and higher in winter, consistent with these estimated seasonal changes in dust concentration. To summarize, it appears that an increase in INP concentration pre-empts the formation of hom cirrus by preventing the RH_i from reaching the threshold for hom,

It can also be argued that the above seasonal differences in the hom fraction can be attributed to seasonal differences in vertical velocities at cirrus cloud levels. This appears likely over the Southern Ocean when one considers the stronger OGWs occurring there during the winter season (Jiang et al., 2002; Hoffmann et al., 2016). Moreover, Gryspeerdt et al. (2018) notes that N_i is higher during winter in the midlatitude storm tracks, consistent with stronger jets. Nonetheless, two studies (Sporre et al., 2022; Lin et al., 2025) have documented large microphysical changes in cirrus clouds that

were affected by volcanic aerosol, which suggests that the observed seasonal differences can be attributed in part to seasonal differences in INP concentrations.

The thick black histograms in the upper panels of Fig. 16 show the zonal mean hom fractions over oceans for DJF (a) and JJA (b). Outside the tropics (±30°), the hom fraction is generally between 10 % and 35 %, although over Antarctica during winter it can be much higher. For comparison, Froyd et al. (2022) estimated the contribution of het and hom to cirrus formation using the dust measurements described above to initialize a detailed cirrus-formation model. They found that het on mineral dust was responsible for 71 % of the cirrus clouds modeled, which is consistent with our findings based exclusively on retrieved cirrus cloud properties. However, comparing Fig. 16 with Fig. 5 and S12 in Froyd et al. (2022) shows that regional differences are larger, where the fraction of hom cirrus in the NH for this study is greater than in Froyd et al. (2022).

3.4.2 Estimating the fraction of het and hom cirrus comprising in situ and warm base cirrus clouds and their estimated radiative impacts

The remote sensing study by Dekoutsidis et al. (2023) found that RH_i values in both in situ and LOC clouds exceed 140 % near cloud top, which is high enough to activate hom. The case studies they examined further underscored the importance of hom in LOC clouds, regardless of whether they were convectively generated or produced through frontal systems (as part of a moisture conveyor belt). The methodology described above for identifying het and hom cirrus clouds was applied to in situ cirrus and WBC clouds. Zonal means of the cloud fractions over oceans are shown in the upper panels of Fig. 16 for DJF (a) and JJA (b), where the thick black histogram separates the het (gray colors) and hom (reddish colors) cirrus cloud regimes. The het fraction is 1 minus the hom fraction. Within these two regimes, the fraction of in situ (IS in the figure) and warm base (WB in the figure) cirrus are indicated. In situ het cirrus are most common, followed by WB het cirrus, although these two cloud types are comparable over the Southern Ocean and Antarctica during summer (DJF). For the hom fraction outside the tropics, the fractions of in situ cirrus and WBC origin clouds are often comparable, although WBC dominates south of 60° S latitude during winter. Although hom in WBC (and thus LOC) has been predicted to occur mostly through the freezing of cloud droplets (Gasparini et al., 2018), evidence for this was not found in Fig. 12 (as discussed in Sect. 3.4.1). Thus, it appears that hom proceeds through the freezing of solution haze droplets for both hom cirrus categories in Fig. 16, making both in situ hom cirrus and hom WBC clouds susceptible to modification by increasing the concentration of INPs, which is the physical basis of CCT (discussed in Sect. 5).

Panels (c) (DJF) and (d) (JJA) of Fig. 16 show for each type of cirrus cloud (i.e., WB hom, IS hom, WB het, IS het) the zonal fraction weighted by optical depth. As in Fig. 1, τ distributions are computed for $\log(\tau)$ between −3 and 1 using bins equal to 0.1 in log space. The τ-weighted fraction of a cirrus type is defined as

$$\tau - \text{weighted fraction (type)} = \frac{\left(\sum_i p_i \cdot \tau_i\right)_{\text{type}}}{\left(\sum_i p_i \cdot \tau_i\right)_{\text{all cirrus}}}, \quad (7)$$

where p_i is the number of pixels in bin τ_i. The τ-weighted fraction of a cirrus type is a proxy for its relative CRE contribution, following the same reasoning given for the CRE proxy in Fig. 1. The thick black histograms in panels (c) and (d) give the relative CRE proxy associated with hom cirrus clouds while the relative contributions from in situ cirrus and WBC clouds to hom cirrus are indicated by the pink and red colors, respectively. Similarly, the relative CRE proxy associated with het cirrus clouds is indicated by the gray colors, with relative contributions from WBC and in situ cirrus indicated by the darker and lighter shades, respectively. The main finding here is that, outside the tropics, the radiative impact of hom cirrus clouds appears comparable to het cirrus clouds. During winter in both hemispheres and over the Southern Ocean in summer, the radiative impact of hom cirrus can even be greater than het cirrus clouds.

3.5 Relating IWC to het and hom cirrus clouds

The results in this study appear generally consistent with those reported in Krämer et al. (2016), titled "A microphysics guide to cirrus clouds – Part 1: Cirrus types" as shown in their Fig. 5 and summarized in their Fig. 9. That study combined measurements of cirrus cloud IWC from 17 aircraft campaigns (94 sampling hours) with predictions of cirrus cloud properties from a detailed microphysical box model. The modeling revealed that the measured median IWC effectively divided cirrus clouds into two updraft (w) regimes; slow (0.01 to 0.1 $\mathrm{m\,s^{-1}}$) and fast (0.5 to 3.0 $\mathrm{m\,s^{-1}}$). The slow w regime where het dominates was characterized by IWC < median IWC, relatively low N_i and relatively large mean mass volume radius R_v. Conversely, the fast w regime where hom dominates was characterized by IWC > median IWC, relatively high N_i and relatively small R_v. Interpreting these w regimes as het and hom regimes, respectively, this study reports similar findings in Figs. 9 and 10 (where α_{ext} correlates strongly with IWC). Figure 17 compares the temperature dependence of the retrieved median IWC (and variance as percentiles) where the median IWC usually lies near the temperature-dependent het–hom transition (shown by the black triangles) as described in Sect. 3.4.1 for cirrus over oceans ($\sim 0.01 < \tau < \sim 3$). In most cases there is a close correspondence between the median IWC and the het–hom transition IWC. The tropics and JJA MID NH are exceptions where the D_e maximum was ambiguous (suggesting hom is less active) and the hom threshold was determined by N_{thres}. Excluding these exceptions, the median IWC tends to partition the het and hom cirrus cloud regimes. This description is

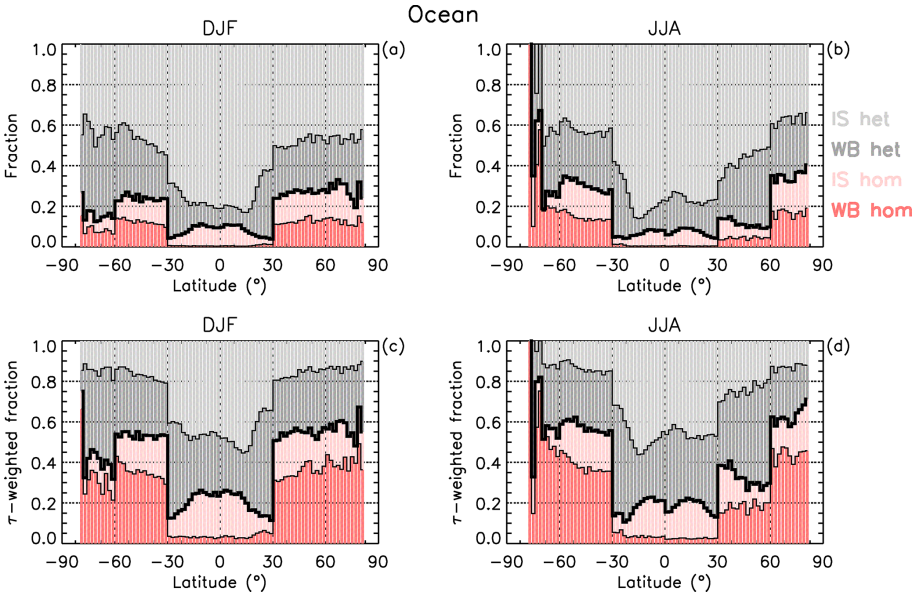

Figure 16. **(a, b)** The fraction of warm base (WB) (red) and in situ (pink) hom-affected cirrus and of WB (dark gray) and in situ (light gray) het cirrus vs. latitude (negative in SH) in **(a)** DJF and **(b)** JJA based on all samples over oceans. The thick black histogram gives the total fraction of hom-affected cirrus. **(c, d)** Same as upper panels except that the fractions are weighted by cloud optical depth (τ).

different from the explanations given in Krämer et al. (2016), where the median IWC roughly separates in situ cirrus from LOC (their Fig. 13).

4 Conceptualizing cirrus cloud formation and evolution

Figure 18 relates median T_r–T_{top} to α_{ext} for various 4 K T_r bins (indicated by the color legend), with the vertical dashed lines giving the α_{ext} at which the corresponding median D_e maximum occurs for the three "warmest" T_r bins. This is done separately for in situ cirrus and WBC clouds. This is based on all IIR samples over the midlatitude oceans, where T_r–T_{top} is related to cloud geometric thickness as discussed earlier. Immediately, it is evident that the in situ cirrus are generally much thinner (geometrically) than the WBC clouds. For the warmest WBC layers (223 K < T < 235 K), it is seen that the correspondence between the D_e maximum and the T_r–T_{top} maximum for a given T_r curve is usually very close; so close that it is hard to dismiss it as a coincidence. For in situ cirrus, this relationship is less evident but begins to emerge in the 223–227 K T bin.

As for the underlying reason accounting for the correspondence between the D_e and T_r–T_{top} maxima in the warmest WBC cloud layers (orange curves), the following is proposed as a working hypothesis for WBC clouds. From Eqs. (24) and (26) in Mitchell (1988), it can be shown that for ice clouds at quasi-steady state conditions, the mean cloud updraft w is directly proportional to the downward ice mass flux χ_f, and since IWC $\approx \chi_f/(v_m - w)$ where v_m is the mass-weighted ice fall speed; IWC is also directly proportional to w when $v_m > w$. As shown in Fig. 17, the het regime increases in IWC as it approaches the het–hom transition region, suggesting an increase in w as well. As w increases (for a given INP concentration), RH_i increases within the cloud until the RH_i reaches the hom threshold. Under quasi-steady state conditions where ice mass produced approximates ice mass removed (e.g., Mitchell, 1994; Field and Heymsfield, 2003), as IWC increases within the het regime, D_e and v_m also increase, exporting ice at higher rates through cloud base. This ice then sublimates, humidifying the sub-cloud layer. Over time this increased sedimentation flux tends to lower cloud base, deepening the cloud. But this cloud deepening ends once hom becomes important, with v_m decreasing due to smaller ice particle sizes. As w (and thus IWC) increase further beyond the het–hom transition, hom becomes more vigorous and D_e further decreases, decreasing v_m and sedimentation rates, showing the evolution of cirrus cloud thickness with increasing cloud updraft and IWC raising cloud base, with geometric cloud thickness becoming minimal at the highest w, IWCs and N_i, and at the lowest D_e, in the hom regime. As cloud layer T_r decreases, ice particle growth rates and mass fluxes through cloud base decrease relative to warmer cloud layers having the same α_{ext}, allowing cloud base to rise, and the curves in Fig. 18 in the het regime become "flatter". Because $T_{base} > 235$ K, the WBC in the het regime become geometrically thicker as T_r decreases. When $T_r < 215$ K, these trends become less coherent presumably due to lower sedimentation rates. This conceptual model for WBC is expected to be most apparent over land where the

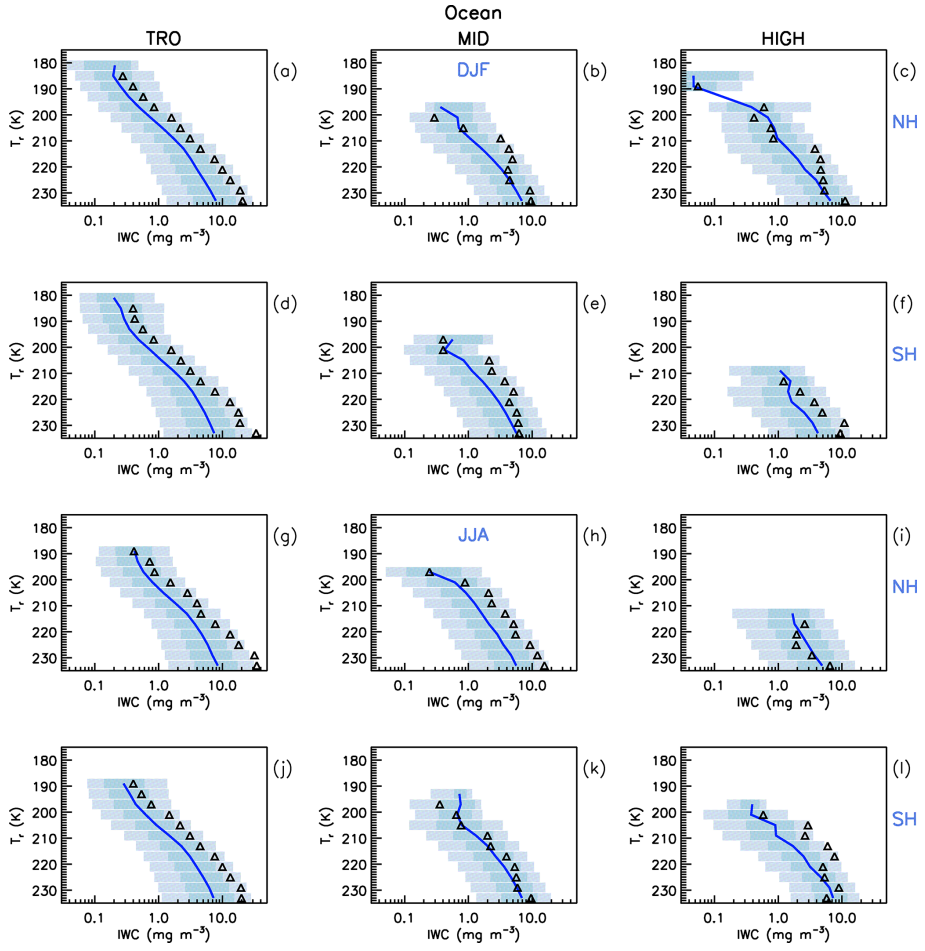

Figure 17. Comparing the median IWC (navy blue curves) over oceans (using all samples) with the temperature-dependent het–hom transition point (black triangles) based on the D_e maximum and the corresponding extinction coefficient α_{ext} for a given 4 K temperature interval. Latitude zones and seasons (DJF and JJA) are denoted as in Figs. 12 and 13. The light-blue shade lies between the 10th and the 90th percentiles and the overplotted medium-blue shade lies between the 25th and 75th percentiles.

hom-regime decrease in D_e (with increasing w and IWC) is more obvious. This simple explanation is consistent with the retrievals of these quantities and T_r–T_{top}. This proposed explanation of Figs. 17 and 18 is summarized in the schematic in Fig. 19 for the warmest WBC layer, presenting a conceptual model of how cirrus cloud thickness might evolve with increasing cloud updraft and IWC for a fixed INP number concentration. Since upward air movements are balanced by downward movements, w in Fig. 19 can be better viewed as the standard deviation of w, σ_w.

For in situ cirrus clouds, $T_{base} \geq 235$ K and when $T_r \approx 233$ K, the clouds are very thin, making it difficult to discern impacts from ice mass sedimentation rates on cloud geometrical depth. This may explain the "flat" nature of these highest temperature curves in Fig. 18. As T_r decreases, cloud depth increases, and for $219 < T_r < 227$ K, the trend observed for warmer WBC clouds is evident, sometimes becoming less coherent for $T_r < 219$ K for reasons similar to WBC clouds.

An Arctic cirrostratus modeling study by Spichtinger and Gierens (2009a, b) simulated hom cirrus where ice nucleation occurred at cloud top, with cirrus beginning as geometrically thin cirrus that rapidly deepen with time (i.e., over the course of an hour). As the cloud deepens, mean N_i (for the cloud layer) decreases since sedimenting and growing ice from cloud top reduces RH_i in the mid- to lower cloud, preventing the RH_i there from reaching the hom threshold. With only het capable of producing new ice crystals in the mid- to lower cloud, mean layer N_i decreases. This appears generally consistent with the above description of hom cirrus and with the upper panel results (a)–(c) in Fig. 6 (where N_i and IWC are lower in the geometrically thicker cirrus). This explanation is also consistent with Fig. A3e–f for $\tau > \sim 0.3$ (where hom cirrus are common), with lower N_i and IWC in the geometrically thicker WBC clouds relative to the thinner in situ cirrus. This "working hypothesis" is speculative and should be tested against other observational datasets and modeling studies.

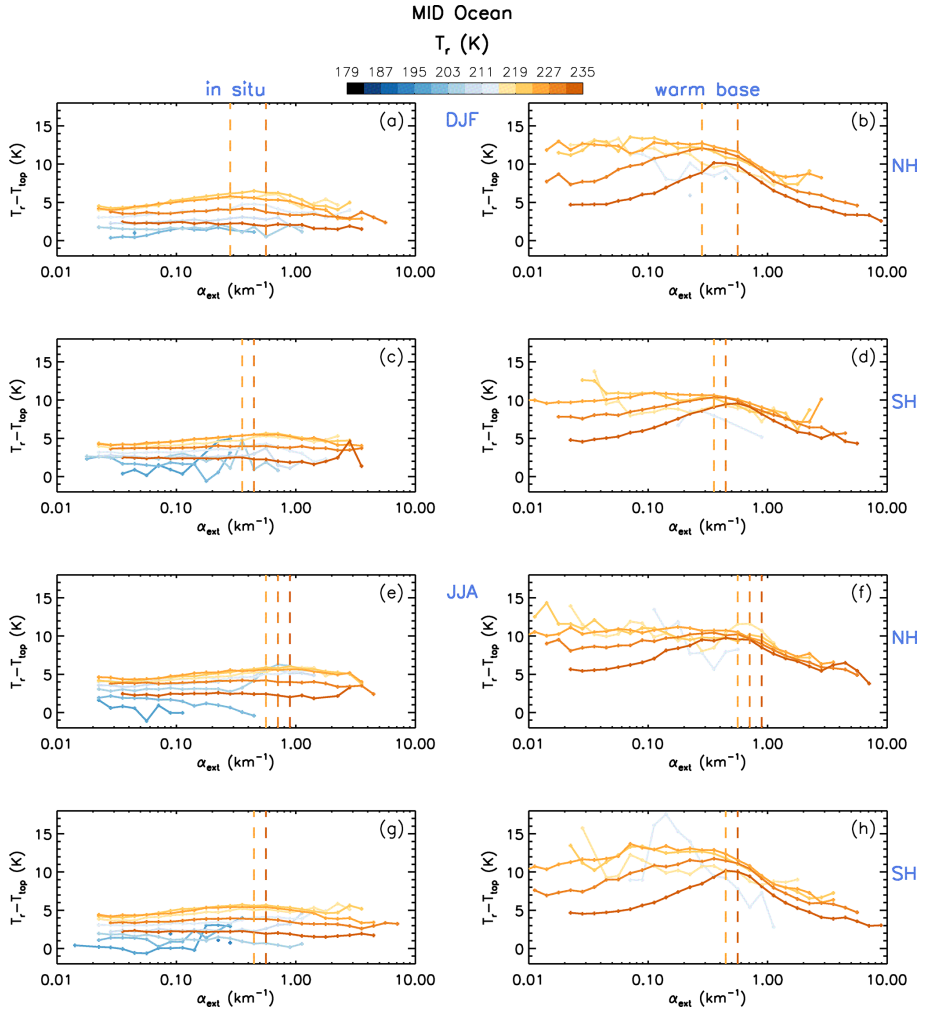

Figure 18. Dependence of T_r–T_{top} (which is related to cirrus cloud geometrical thickness) on the extinction coefficient α_{ext} for various 4 K temperature bins indicated by the color bar. Retrievals were over oceans ($\sim 0.01 < \tau < \sim 3$) for in situ cirrus **(a, c, e, g)** and WBC **(b, d, f, h)** clouds at midlatitude for two seasons (DJF and JJA) in both hemispheres (NH and SH) during 2008, 2010, 2012, and 2013. Vertical lines indicate D_e maxima for the three "warmest" temperature bins, revealing a correspondence between cloud thickness and D_e maxima. Panels having only two vertical lines result from two D_e maxima having the same α_{ext}.

5 Implications for cirrus cloud representations in climate models and cirrus cloud thinning

Climate modeling investigations into the climate intervention method known as cirrus cloud thinning or CCT have exposed our lack of understanding about cirrus clouds. CCT is based on the principle that hom cirrus can be seeded with higher INP concentrations (relative to ambient) to convert them to het cirrus. This would allow more outgoing longwave radiation to escape to space since a conversion to het cirrus would (1) reduce the cirrus cloud τ and lifetime (due to larger ice crystals falling faster), (2) cause the cirrus to form at lower altitudes (since the augmented INP require lower RH_i to nucleate) where their warming effect is weaker, and (3) the enhanced ice sedimentation rates would enhance the removal of water vapor (a powerful greenhouse gas) from the UT (Mitchell and Finnegan, 2009; Lohmann and Gasparini, 2017). Thus, the physical processes affecting CCT are complex and difficult to model, and numerous CCT modeling studies have produced mixed results, with some predicting a cooling effect (Storelvmo et al., 2013; Storelvmo and Herger, 2014; Storelvmo et al., 2014; Gruber et al., 2019; Gasparini et al., 2020; Liu and Shi, 2021; Muri et al., 2014; Crook et al., 2015; Kristjánsson et al., 2015; Jackson et al., 2016; Cao et al., 2017; Muri et al., 2018; Duan et al., 2018, 2020) and others predicting a negligible or warming effect regarding the CCT net CRE (Penner et al., 2015; Gasparini and Lohmann, 2016; Gasparini et al., 2017; Tully et al., 2022, 2023). But perhaps the greatest uncertainty in these studies is the role of hom in cirrus cloud formation, since if hom is not an important process, no significant cooling from CCT is possible. To quote Lohmann and Gasparini (2017), "For the time being,

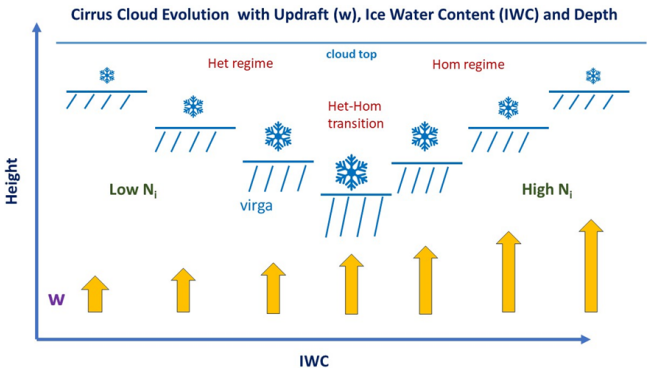

Figure 19. Proposed evolution of cirrus cloud thickness or depth with increasing cloud updraft (arrows) and IWC, based on results in Figs. 17 and 18 for the warmest WBC cloud layers. The relative cloud depth is the height difference between the cloud top line and the line segments below (with virga shown below these line segments). The size of the ice crystal symbol represents the relative size of D_e. As D_e increases, sedimentation or virga increases, lowering cloud base. Hom acts to decrease D_e, decreasing sedimentation and thus raising cloud base.

cirrus cloud thinning should be viewed as a thought experiment that is helping to understand cirrus cloud–formation mechanisms". Similarly, the United Nations Environment Programme (2023) titled "One Atmosphere: An independent expert review on Solar Radiation Modification research and deployment" states, "The feasibility of CCT is uncertain, in part because of the larger uncertainties associated with the ice nucleation processes in high clouds". Both reports are indicating that the relative role of het and hom is the key issue determining the viability of CCT. This CALIPSO study is relevant to CCT because it evaluates the relative role of het and hom as a function of temperature, latitude, season and topography in terms of cloud fraction and radiative impact. Since this study found that the radiative contribution of hom cirrus is substantial, an attempt to improve the treatment of cirrus cloud microphysics in CCT modeling experiments is given below.

The CCT simulations that use the treatment of pre-existing ice (Shi et al., 2015) tend to predict a relatively small or no CCT cooling effect while those CCT simulations that do not use this pre-existing ice treatment predict a substantial cooling (Gasparini et al., 2020; Tully et al., 2023). The pre-existing ice treatment described in Shi et al. (2015) is based on the supersaturation development equation that can be written as

$$\frac{dS_i}{dt} = a_1 S_i W - (a_2 + a_3 S_i)\left(\frac{dq_{i,\,nuc}}{dt} + \frac{dq_{i,\,pre}}{dt}\right), \quad (8)$$

where $q_{i,\,nuc}$ is the ice mass mixing ratio due to ice nucleation and $q_{i,\,pre}$ is the ice mass mixing ratio of pre-existing ice, parameters a_1, a_2 and a_3 depend only on the ambient temperature and pressure, S_i is the supersaturation with respect to ice, W is the updraft velocity and t is time. From this equation it is seen that the greater $q_{i,\,pre}$ is, the smaller the increase in S_i. The study by Dekoutsidis et al. (2023) indicates that hom occurs in a relatively thin layer near cloud top, and the study by Diao et al. (2015) shows that ice nucleation in cirrus occurs near cloud top. This suggests that $q_{i,\,pre}$ may be overestimated in GCMs since $q_{i,\,pre}$ is based on layer mean IWC or q_i values, whereas the actual $q_{i,\,pre}$ should correspond to a relatively thin layer near cloud top that the vertical resolution in a climate model cannot accommodate. When $q_{i,\,pre}$ is overestimated, it is much more difficult for S_i to reach the threshold for hom. As stated in Shi et al. (2015), "The pre-existing ice crystals significantly reduce ice number concentrations in cirrus clouds, especially at mid- to high latitudes in the UT (by a factor of ~ 10). Furthermore, the contribution of heterogeneous ice nucleation to cirrus ice crystal number increases considerably." That is, CCT modeling experiments that predict a relatively small hom fraction and thus negligible cooling have used a pre-existing ice treatment (e.g., Gasparini and Lohmann, 2016). To address this issue, the model's vertical resolution could be increased, or $q_{i,\,pre}$ could be attenuated by a factor that best represents q_i near cloud top in the "nucleation zone". The global/seasonal distribution of the predicted hom fraction could be compared against results from this CALIPSO study.

The Community Atmosphere Model Version 6 (i.e., CAM6) uses the standard treatment of pre-existing ice, and also considers turbulence kinetic energy as the only dynamic source for in situ ice formation (Lyu et al., 2023). That is, OGWs are not considered in ice nucleation. Lyu et al. (2023) demonstrated the importance of including OGWs in CAM6, which triggered more frequent hom in orographic cirrus, increasing N_i and IWC while decreasing D_e.

The impact of OGWs on cirrus clouds is evaluated in Appendix A of Tully et al. (2022), where a version of the ECHAM6-HAM GCM is used. Figure A3 of that paper evaluates N_i at 200 hPa for vertical motions with and without orographic effects active. When orographic effects are included, predicted global distributions of N_i appear similar to Fig. S5 of this study featuring N_i for in situ cirrus clouds. An example of what OGW cirrus clouds often look like is given in Fig. 20; they are usually optically thicker than het cirrus clouds. Cirrus clouds induced by OGWs, often called wave cirrus, have relatively high updrafts and thus are more likely to be hom cirrus clouds (Barahona and Nenes, 2008; Joos et al., 2008, 2014; Barahona et al., 2017; Lyu et al., 2023; M2018). They also tend to exhibit higher cloud fractions (see Fig. 4 in Matus and L'Ecuyer, 2017). These OGW cirrus are characterized by relatively high N_i (M2018; Gryspeerdt et al., 2018) and, perhaps due to the oscillation of the OGW, are evident far downwind from mountain ranges in North America, Patagonia and Antarctica during winter (see Figs. 2 and S5). Note that hom cirrus are not restricted to OGW cirrus and may form under other conditions having relatively high updrafts and/or low INP concentrations.

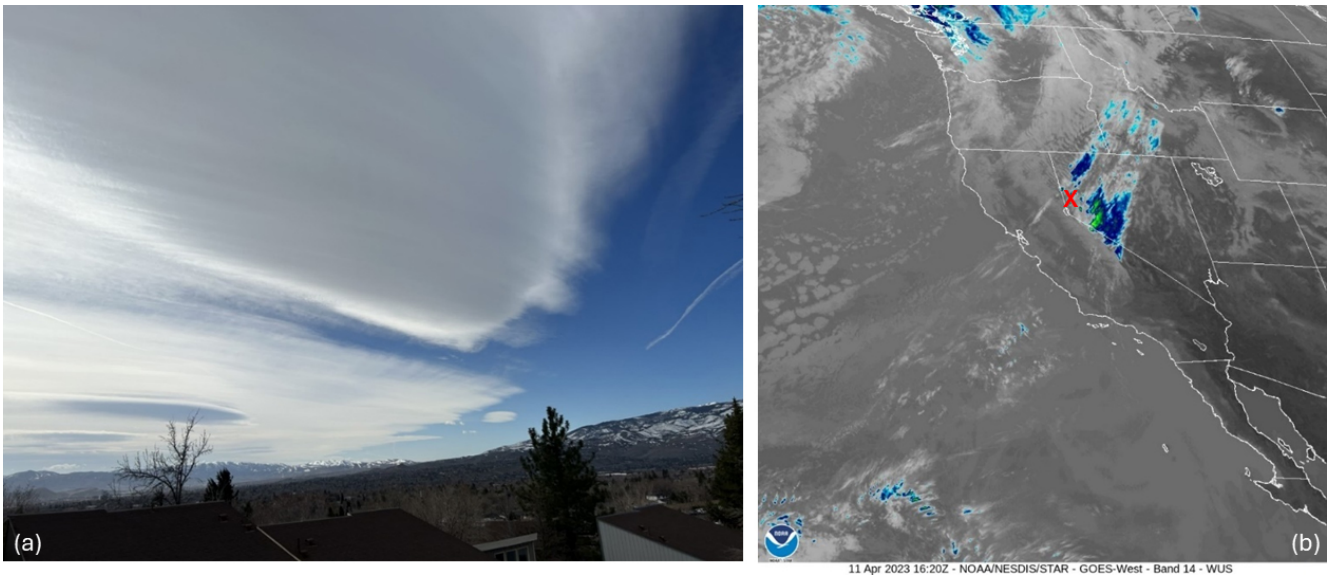

Figure 20. **(a)** A wave cloud example of hom cirrus, forming over the Sierra Nevada mountains next to Reno, Nevada, that are associated with a warm front on 11 April 2023. **(b)** GOES-18 satellite image (11.2 µm channel) of these cirrus wave clouds acquired about 10 min before the photo was taken, revealing their extensive coverage. Low clouds are white-gray while high clouds (e.g., blue colors) tend to have lower brightness temperatures (BT), with lowest BT in dark blue and green. The red "X" indicates the location of the cloud scene in the photo.

CCT is potentially most effective at high latitudes during autumn and winter when solar insolation is relatively weak (Storelvmo et al., 2014; Mitchell et al., 2020). Based on this study, CCT could have a cooling effect at high latitudes based on the τ-weighted hom fraction. But this cooling could be compromised by a corresponding warming effect resulting from (1) a het cirrus Twomey effect (i.e., where higher INP concentrations produce higher N_i and smaller D_e) and (2) a het cirrus IWC/IWP effect (i.e., where smaller D_e from the Twomey effect produce lower fall speeds, increasing the IWC and IWP as demonstrated in Mitchell et al., 2008). These two effects may increase τ and cloud lifetime (Mitchell et al., 2008), increasing the warming effect of het cirrus clouds during Arctic winter. The two opposing radiative effects resulting from higher INP concentrations, the hom cirrus cooling effect and the het cirrus warming effect, need to be investigated by empowering climate modeling with satellite observations like these to better understand aerosol-cirrus cloud-climate interactions. Moreover, radiative transfer models may employ the CALIPSO retrievals presented here to better understand INP-cirrus cloud-radiation interactions, but these topics are beyond the scope of this study.

6 Summary and conclusions

This study dealt with the identification of relevant cloud physical parameters to identify hom-affected cirrus clouds and further quantify their frequency of occurrence. From a global observational purview, this was done for the first time by Froyd et al. (2022) who used global measurements of dust concentration from aircraft in the UT to initialize a detailed cirrus cloud formation model that used reanalysis data in the dust trajectory simulations. In contrast, our study is based on retrieved cirrus cloud properties and does not involve modeling. In addition, our study estimates the relative radiative impact of het and hom cirrus clouds through the τ-weighted hom fraction.

In Sect. 2, global-seasonal maps for optically thick cirrus clouds ($\sim 0.3 < \tau < \sim 3$) show relatively high N_i and relatively low D_e at high latitudes during winter, especially over mountainous terrain. OGWs induced by mountains provide stronger updrafts that promote hom, which may help explain these results. Gryspeerdt et al. (2018) and M2018 reported similar findings and explanations. This winter phenomenon was also observed at midlatitudes over mountainous regions. Similar maps for IWC and T_r show that IWC tends to track T_r, consistent with expectations from the Clausius–Clapeyron equation. Similar maps of N_i and D_e restricted to in situ cirrus exhibit these same patterns but with higher N_i and smaller D_e, possibly resulting from their lower temperatures and lower geometrical thickness as described in Sect. 4.

The attribution study of het and hom-affected cirrus clouds (Sect. 3) began with determining which cloud properties were most sensitive to hom by exploiting a finding that hom was most active (based on N_i) in the geometrically thinnest cirrus clouds (i.e., having the smallest T_r–T_{top}). Other than N_i, IWC was most sensitive to hom (with IWC increasing with hom activity), followed by D_e (mostly over land, with D_e decreasing with increasing hom activity). Therefore, the

extinction coefficient α_{ext} for visible radiation was used to separate het and hom cirrus clouds since α_{ext} includes the IWC / D_e ratio. Comparisons of our retrievals of N_i, IWC and D_e in the T_r vs. α_{ext} space with predicted corresponding values for pure hom conditions (based on the Clausius–Clapeyron equation and simple hom theory) revealed that maximum retrieved values for IWC and N_i (for a given T_r) coincided with theory, verifying the success of α_{ext} for separating het- and hom-affected cirrus clouds (as well as validating the retrievals).

With this understanding, a method was developed to quantify the contribution of cirrus clouds affected by hom. This involved analyzing variations of D_e against $\log(\alpha_{ext})$ where D_e exhibited a maximum typically at $\alpha_{ext} > 0.3\,km^{-1}$ for $T_r = 233\,K$, with the maxima tending to occur at lower α_{ext} with decreasing T_r. This D_e maximum was interpreted as a transition from het cirrus to hom-affected cirrus, with D_e decreasing with increasing α_{ext} in the hom regime due to higher N_i resulting from hom. That is, the greater competition for water vapor due to higher N_i in the hom regime reduces ice crystal growth rates, reducing D_e with increasing N_i. This method ensures that hom always has an unambiguous impact on cloud microphysical and radiative properties. Most of the quantitative results are over oceans where retrieval uncertainties are smaller than over land, owing to smaller uncertainties in surface parameters. The main findings of this het–hom attribution study are as follows:

1. Outside the tropics over oceans, zonal means of the fraction of hom-affected cirrus clouds during winter were generally between 25 % and 30 %, with a comparable contribution from in situ cirrus and warm base cirrus clouds, similar to the findings of Dekoutsidis et al. (2023).

2. The relative contribution of hom-affected cirrus in terms of radiation impact was estimated using a proxy for the net CRE inferred from τ distributions as a τ-weighted occurrence frequency. Using this proxy, we found that optically thick cirrus clouds with $0.3 < \tau < 3$ represent 78 % to 87 % of the radiative weight for all cirrus clouds sampled depending on latitude, which compared favorably with results from Hong et al. (2016). Using this proxy, the τ-weighted fraction for hom-affected cirrus over oceans outside the tropics during winter was > 50 %, indicating that hom cirrus may contribute substantially to the Earth's radiation budget.

3. Based on two earlier studies that evaluate mineral dust contributions from the main dust source regions to different latitude zones during different seasons, the fraction of hom cirrus was lowest downwind of the Asian dust source regions during summer when UT dust concentrations were highest. Similarly, the fraction of hom cirrus over the Southern Ocean was lowest during summer when dust concentrations were highest (relative to winter). This suggests that the hom fraction is sensitive to mineral dust concentration and this may be a natural analogue to the climate intervention proposal known as cirrus cloud thinning (Mitchell and Finnegan, 2009). However, these seasonal changes in the hom cirrus fraction might partly be explained by seasonal changes in vertical velocities.

4. Hom-affected cirrus were found to have a median N_i typically $\geq 200\,L^{-1}$ (see Fig. 12) and τ is much larger than in het cirrus (Fig. 13). To a first approximation, the median IWC divides the het and hom cirrus cloud regimes outside the tropics (Fig. 17).

5. When plotting D_e and T_r–T_{top} against α_{ext}, it was found that their maxima occurred at approximately the same α_{ext}. A simple theory of cirrus cloud development was postulated to explain this observation.

6. Contrasting N_i and D_e vs. α_{ext} plots for oceans and land in the het regime, it appears that higher INP over land may be producing a Twomey effect in het cirrus clouds over land. However, in the hom regime, higher INP concentrations appear to reduce the hom fraction and thus substantially reduce cirrus cloud optical depth.

Appendix A: Global distributions and properties of in situ and liquid origin cirrus clouds

Figure A1 shows the geographic sampling distribution of $1\,km^2$ IIR pixels for two periods: DJF and JJA. Optically thick cirrus that can be measured over both land and oceans are featured in the panels (a)–(b) while sample counts for all cirrus over oceans with valid retrieved effective emissivities at both 10.6 and 12.05 µm ($\sim 0.01 < \tau < \sim 3$) are featured in panels (c)–(d). The higher counts in panels (c)–(d) are mostly due to in situ cirrus clouds.

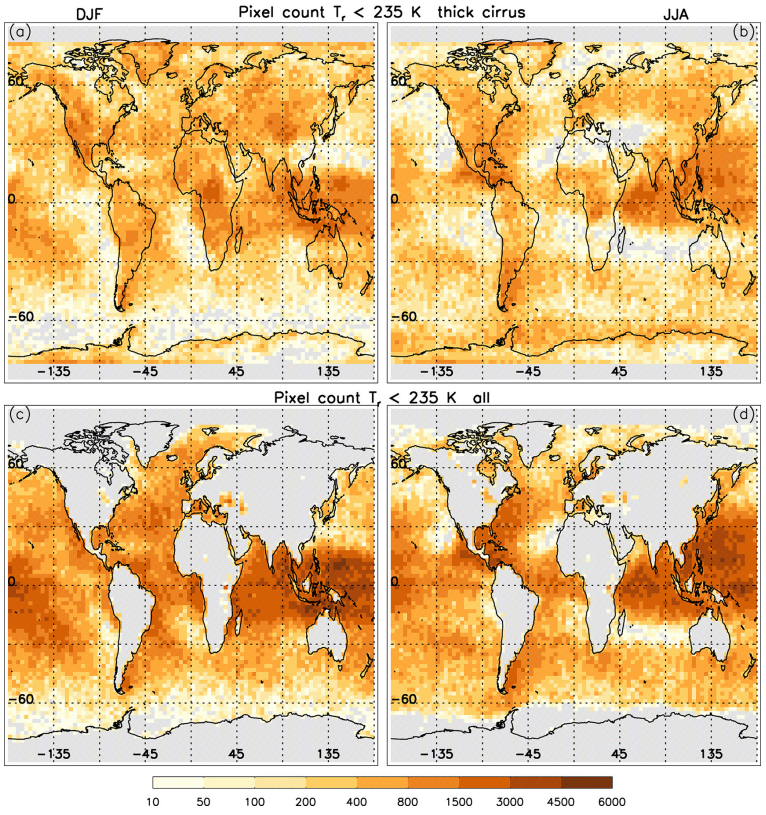

Figure A1. Geographic sampling distribution of optically thick cirrus clouds during DJF **(a)** and JJA **(b)**, where the number of sample counts is given by the color bar. Similarly, this sampling distribution is given for all cirrus clouds over oceans only ($\sim 0.01 < \tau < \sim 3$) during DJF **(c)** and JJA **(d)**. Analysis for years 2008, 2010, 2012, and 2013.

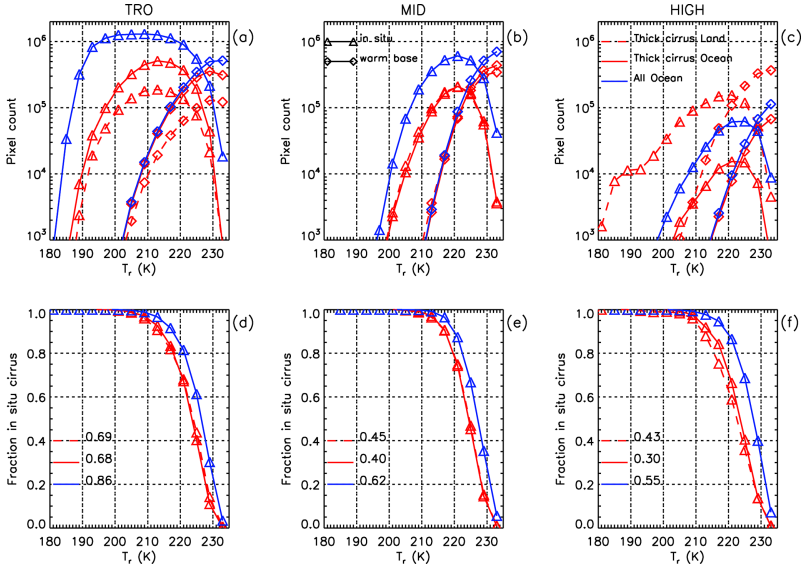

Figure A2. **(a–c)** Global annual mean radiative temperature distributions of sampled in situ (triangles) and warm base (diamonds) cirrus clouds arranged horizontally by latitude zone: **(a)** tropics, **(b)** mid- and **(c)** high latitudes, NH and SH combined. Distributions were built with a 4 K temperature step. Red curves indicate optically thick clouds over land (dashed) and oceans (solid), while blue curves show results for all samples over oceans. **(d–f)** Red curves show the fraction of in situ cirrus clouds derived from upper panel results for optically thick clouds over land (dashed) and oceans (solid) while blue curves show the same but for all samples over oceans only. Numbers indicate the overall fraction of in situ cirrus clouds for each cloud category (indicated by corresponding line pattern or color). Analysis for years 2008, 2010, 2012, and 2013.

Figure A2a–c shows the abundance of in situ and warm base cirrus (WBC) as a function of cloud radiative temperature T_r for three latitude bands (combining NH and SH results), discriminating between optically thick cirrus (1) over land and (2) over oceans ($\sim 0.3 < \tau < \sim 3$) and (3) all retrieved cirrus clouds over oceans ($\sim 0.01 < \tau < \sim 3$). Figure A2d–f shows the fraction of in situ cirrus clouds $\left[\text{in situ}/(\text{in situ} + \text{WBC})\right]$ as a function of T_r. The overall (total) fraction of in situ cirrus clouds for the above three cloud classes is indicated in each panel by the fraction and adjacent line pattern (or color). Temperature bins are 4 K resolution. Note that we count 1 km^2 IIR pixels, and that a cirrus cloud extending 20 km horizontally along a portion of the lidar track is counted 20 times whereas a cirrus cloud extending 5 km along this track is counted only five times. Using the above definitions, Fig. A2d–f shows that the fraction of all retrieved in situ cirrus clouds over oceans reaches ~ 50 % for $T_r \approx 227$ K for all latitude zones. These findings can be compared with those reported in Fig. 4 of Dekoutsidis et al. (2023) over Europe, where it is evident that the occurrence of in situ cirrus prevails over LOC for $T_r < 221$ K. Similarly, Fig. 13 in Luebke et al. (2016) shows that for Europe, the transition from in situ cirrus dominating to LOC dominating occurs between 218 and 222 K. These studies are fairly consistent with this one given the different methods used to discriminate between in situ cirrus and either LOC or WBC clouds. As noted in Sect. 2.1, our method may overestimate the occurrence frequency of in situ cirrus clouds. From Fig. A2, the overall percentage of in situ cirrus for all sampled cirrus over oceans ranges from 86 % in the tropics, to 62 % in the midlatitudes, and 55 % in the high latitudes. These percentages, subtracted from 100, yield the percentage of WBC clouds.

A major motivation for investigating these two types of cirrus cloud is that their probable different origins may endow them with different microphysical and radiative properties. While our cloud classification method (in situ vs. WBC) was not designed for evaluating the cloud's microphysical origin (i.e., using back-trajectory analysis) like the in situ-LOC classification was, it may be sufficiently similar to capture some of the microphysical distinctions observed between the in situ and LOC classifications. This assumption is tested in Fig. A3 which contrasts the T_r dependence of N_i, D_e and IWC for in situ and WBC clouds over oceans for two τ classes: (1) $0.01 < \tau < 3$ and (2) $0.3 \leq \tau \leq 3$, where (1) is for all IIR samples and (2) provides the lowest uncertainties. This analysis is for winter at 30–60° N latitude. Class (1) may be more representative of aircraft measurements that do not discriminate between thin and thick cirrus, while class (2) is for relatively optically thick cirrus. These results are discussed in the last paragraph of Sect. 2.3. Based on all samples over oceans (blue curves), the main differences between in situ cirrus and WBC clouds are their IWPs and τ, which are greater for WBC clouds. The geometric thickness (Δz) in Fig. A3d is the vertical geometrical thickness of the cloud layer measured by CALIOP while the IIR equivalent thickness (Δz_{eq}, panel c) accounts for the fact that the IIR instrument does not equally sense all of the cloud profile that contribute to thermal emission (M2018; Garnier et al., 2021; M2025). This is accounted for through the IIR weighting profile as illustrated in M2025, which gives more weight to higher extinctions in the cloud profile. Both median Δz and Δz_{eq} are larger for WBC, partly explaining their higher IWPs and τ. As shown in Fig. 12, the temperature dependence of the fraction of hom cirrus varies with latitude and season, indicating that results in Fig. A3 may vary somewhat for different latitude zones and seasons.

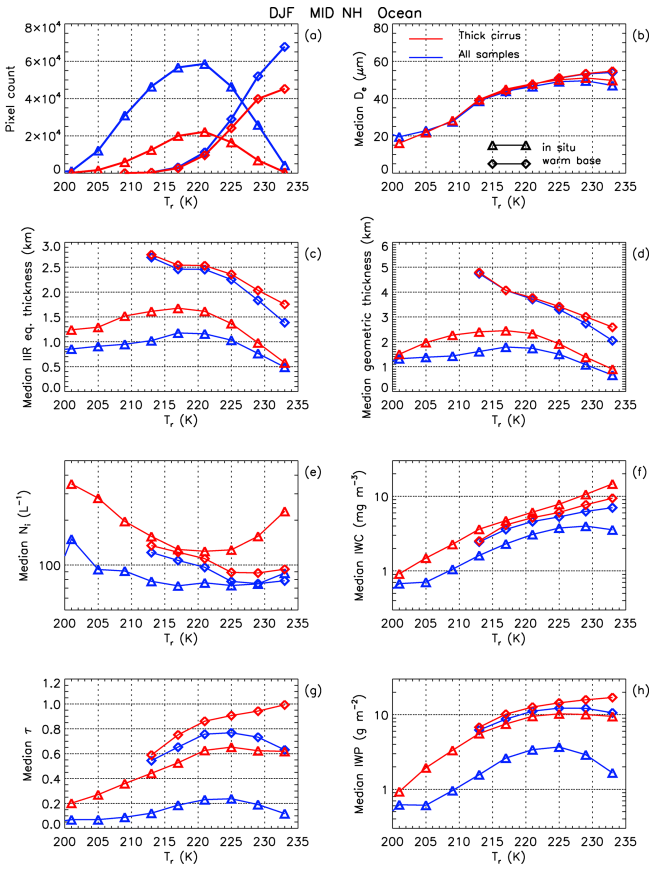

Figure A3. Retrieval results contrasting in situ (triangle symbols) with warm base (diamond symbols) cirrus cloud properties for the NH midlatitudes over oceans during DJF. The blue curves are based on all samples ($\sim 0.01 < \tau < \sim 3$) while the red curves are for optically thick cirrus clouds ($\sim 0.3 < \tau < \sim 3$). Shown for each cirrus cloud type and range of τ are **(a)** number of retrieval samples, **(b)** median D_e (μm), **(c)** median IIR equivalent thickness (km), **(d)** median geometric thickness (km), **(e)** median N_i (L^{-1}), **(f)** median IWC (mg m^{-3}), **(g)** median τ, and **(h)** median IWP (g m^{-2}).

Data availability. The CALIPSO IIR Level 2 data products used in this study are available at the NASA Langley Atmospheric Science Data Center and can be retrieved from https://doi.org/

10.5067/IIR/CALIPSO/CAL_IIR_L2_Track-Standard-V4-51 (NASA/LARC/SD/ASDC, 2023a). The CALIPSO Lidar Level 2 cloud profiles used in this study are available at the NASA Langley Atmospheric Science Data Center and can be retrieved from https://doi.org/10.5067/CALIOP/CALIPSO/CAL_LID_L2_05kmCPro-Standard-V4-51 (NASA/LARC/SD/ASDC, 2023b). These CALIPSO data products are also available from the AERIS/ICARE Data and Services Center in France (https://www.icare.univ-lille.fr/, last access: 11 October 2025). Post-processed data are available upon request to the authors.

Supplement. The supplement related to this article is available online at https://doi.org/10.5194/acp-25-14099-2025-supplement.

Author contributions. DM and AG conceived the study; DM contributed to the writing of the paper; AG accessed and analyzed the CALIPSO data and contributed to the writing of the paper.

Competing interests. The contact author has declared that neither of the authors has any competing interests.

Disclaimer. Publisher's note: Copernicus Publications remains neutral with regard to jurisdictional claims made in the text, published maps, institutional affiliations, or any other geographical representation in this paper. While Copernicus Publications makes every effort to include appropriate place names, the final responsibility lies with the authors.

Acknowledgements. This research was supported by NOAA (grant no. NA22OAR4690640) and by the NASA CALIPSO project. The authors are grateful to the Centre National d'Etudes Spatiales (CNES) and to the AERIS/ICARE Data and Services Center in France for their support with the CALIPSO IIR data. We are grateful to Martina Krämer for asking us to produce Fig. 17. We also thank Ehsan Erfani for his assistance with the SPARTICUS data analysis and for his participation and suggestions in scientific discussions. The authors extend their gratitude to the two reviewers who have contributed important content to this study.

Financial support. This research has been supported by the National Oceanic and Atmospheric Administration (NOAA; grant no. NA22OAR4690640) and the NASA Science Mission Directorate (CALIPSO Project).

Review statement. This paper was edited by Matthias Tesche and reviewed by Blaž Gasparini and one anonymous referee.

References

Avery, M. A., Ryan, R. A., Getzewich, B. J., Vaughan, M. A., Winker, D. M., Hu, Y., Garnier, A., Pelon, J., and Verhappen, C. A.: CALIOP V4 cloud thermodynamic phase assignment and the impact of near-nadir viewing angles, Atmos. Meas. Tech., 13, 4539–4563, https://doi.org/10.5194/amt-13-4539-2020, 2020.

Barahona, D. and Nenes, A.: Parameterization of cirrus cloud formation in large-scale models: Homogeneous nucleation, J. Geophys. Res., 113, D11211, https://doi.org/10.1029/2007JD009355, 2008.

Barahona, D. and Nenes, A.: Parameterizing the competition between homogeneous and heterogeneous freezing in ice cloud formation – polydisperse ice nuclei, Atmos. Chem. Phys., 9, 5933–5948, https://doi.org/10.5194/acp-9-5933-2009, 2009.

Barahona, D., Molod, A., and Kalesse, H.: Direct estimation of the global distribution of vertical velocity within cirrus clouds, Sci. Rep., 7, 6840, https://doi.org/10.1038/s41598-017-07038-6, 2017.

Cao, L., Duan, L., Bala, G., and Caldeira, K.: Simultaneous stabilization of global temperature and precipitation through cocktail geoengineering, Geophys. Res. Lett., 44, 7429–7437, https://doi.org/10.1002/2017GL074281, 2017.

Carlsen, T. and David, R. O.: Spaceborne evidence that ice-nucleating particles influence high-latitude cloud phase, Geophys. Res. Lett., 49, e2022GL098041, https://doi.org/10.1029/2022GL098041, 2022.

Costa, A., Meyer, J., Afchine, A., Luebke, A., Günther, G., Dorsey, J. R., Gallagher, M. W., Ehrlich, A., Wendisch, M., Baumgardner, D., Wex, H., and Krämer, M.: Classification of Arctic, midlatitude and tropical clouds in the mixed-phase temperature regime, Atmos. Chem. Phys., 17, 12219–12238, https://doi.org/10.5194/acp-17-12219-2017, 2017.

Creamean, J. M., Kirpes, R. M., Pratt, K. A., Spada, N. J., Maahn, M., de Boer, G., Schnell, R. C., and China, S.: Marine and terrestrial influences on ice nucleating particles during continuous springtime measurements in an Arctic oilfield location, Atmos. Chem. Phys., 18, 18023–18042, https://doi.org/10.5194/acp-18-18023-2018, 2018.

Crook, J. A., Jackson, L. S., Osprey, S. M., and Forster, P. M.: A comparison of temperature and precipitation responses to different Earth radiation management geoengineering schemes, J. Geophys. Res., 120, 9352–9373, https://doi.org/10.1002/2015JD023269, 2015.

Danielsen, E. F.: In situ evidence of rapid, vertical, irreversible transport of lower tropospheric air into the lower tropical stratosphere by convective cloud turrets and by larger-scale upwelling in tropical cyclones, J. Geophys. Res., 98, 8665–8681, https://doi.org/10.1029/92JD02954, 1993.

Dekoutsidis, G., Groß, S., Wirth, M., Krämer, M., and Rolf, C.: Characteristics of supersaturation in midlatitude cirrus clouds and their adjacent cloud-free air, Atmos. Chem. Phys., 23, 3103–3117, https://doi.org/10.5194/acp-23-3103-2023, 2023.

Diao, M., Jensen, J. B., Pan, L. L., Homeyer, C. R., Honomichl, S., Bresch, J. F., and Bansemer, A.: Distributions of ice supersaturation and ice crystals from airborne observations in relation to upper tropospheric dynamical boundaries, J. Geophys. Res.-Atmos., 120, 5101–5121, https://doi.org/10.1002/2015JD023139, 2015.

Duan, L., Cao, L., Bala, G., and Caldeira, K.: Comparison of the fast and slow climate response to three radiation management geoengineering schemes, J. Geophys. Res.-Atmos., 123, 11980–12001, https://doi.org/10.1029/2018JD029034, 2018.

Duan, L., Cao, L., Bala, G., and Caldeira, K.: A model-based investigation of terrestrial plant carbon uptake response to four radiation modification approaches, J. Geophys. Res.-Atmos., 125, e2019JD031883, https://doi.org/10.1029/2019JD031883, 2020.

Emde, C., Buras-Schnell, R., Kylling, A., Mayer, B., Gasteiger, J., Hamann, U., Kylling, J., Richter, B., Pause, C., Dowling, T., and Bugliaro, L.: The libRadtran software package for radiative transfer calculations (version 2.0.1), Geosci. Model Dev., 9, 1647–1672, https://doi.org/10.5194/gmd-9-1647-2016, 2016.

Erfani, E. and Mitchell, D. L.: Developing and bounding ice particle mass- and area-dimension expressions for use in atmospheric models and remote sensing, Atmos. Chem. Phys., 16, 4379–4400, https://doi.org/10.5194/acp-16-4379-2016, 2016.

Field, P. R. and Heymsfield, A. J.: Aggregation and Scaling of Ice Crystal Size Distributions, J. Atmos. Sci., 60, 544–560, https://doi.org/10.1175/1520-0469(2003)060<0544:AASOIC>2.0.CO;2, 2003.

Froyd, K. D., Yu, P. F., Schill, G. P., Brock, C. A., Kupc, A., Williamson, C. J., Jensen, E. J., Ray, E., Rosenlof, K. H., Bian, H. S., Darmenov, A. S., Colarco, P. R., Diskin, G. S., Bui, T., and Murphy, D. M.: Dominant role of mineral dust in cirrus cloud formation revealed by global-scale measurements, Nat. Geosci., 15, 177–183, https://doi.org/10.1038/s41561-022-00901-w, 2022.

Garnier, A., Pelon, J., Pascal, N., Vaughan, M. A., Dubuisson, P., Yang, P., and Mitchell, D. L.: Version 4 CALIPSO Imaging Infrared Radiometer ice and liquid water cloud microphysical properties – Part I: The retrieval algorithms, Atmos. Meas. Tech., 14, 3253–3276, https://doi.org/10.5194/amt-14-3253-2021, 2021.

Gasparini, B. and Lohmann, U.: Why cirrus cloud seeding cannot substantially cool the planet, J. Geophys. Res., 121, 4877–4893, https://doi.org/10.1002/2015JD024666, 2016.

Gasparini, B., Münch, S., Poncet, L., Feldmann, M., and Lohmann, U.: Is increasing ice crystal sedimentation velocity in geoengineering simulations a good proxy for cirrus cloud seeding?, Atmos. Chem. Phys., 17, 4871–4885, https://doi.org/10.5194/acp-17-4871-2017, 2017.

Gasparini, B., Meyer, A., Neubauer, D., Münch, S., and Lohmann, U.: Cirrus Cloud Properties as Seen by the CALIPSO Satellite and ECHAM-HAM Global Climate Model, J. Climate, 31, 1983–2003, https://doi.org/10.1175/JCLI-D-16-0608.1, 2018.

Gasparini, B., McGraw, Z., Storelvmo, T., and Lohmann, U.: To what extent can cirrus cloud seeding counteract global warming?, Environ. Res. Lett., 15, 054002, https://doi.org/10.1088/1748-9326/ab71a3, 2020.

Gelaro, R., McCarty, W., Suárez, M. J., Todling, R., Molod, A., Takacs, L., Randles, C. A., Darmenov, A., Bosilovich, M. G., Reichle, R., Wargan, K., Coy, L., Cullather, R., Draper, C., Akella, S., Buchard, V., Conaty, A., da Silva, A. M., Gu, W., Kim, G., Koster, R., Lucchesi, R., Merkova, D., Nielsen, J. E., Partyka, G., Pawson, S., Putman, W., Rienecker, M., Schubert, S. D., Sienkiewicz, M., and Zhao, B.: The Modern-Era Retrospective Analysis for Research and Applications, Version 2 (MERRA-2), J. Climate, 30, 5419–5454, https://doi.org/10.1175/JCLI-D-16-0758.1, 2017.

Gettelman, A., Liu, X., Ghan, S. J., Morrison, H., Park, S., Conley, A. J., Klein, S. A., Boyle, J., Mitchell, D. L., and Li, J.-L. F.: Global simulations of ice nucleation and ice supersaturation with an improved cloud scheme in the community atmosphere model, J. Geophys. Res., 115, D18216, https://doi.org/10.1029/2009JD013797, 2010.

Gettelman, A., Liu, X., Barahona, D., Lohmann, U. and Chen, C.: Climate impacts of ice nucleation, J. Geophys. Res., 117, D20201, https://doi.org/10.1029/2012JD017950, 2012.

Gruber, S., Blahak, U., Haenel, F., Kottmeier, C., Leisner, T., Muskatel, H., Storelvmo, T. and Vogel, B.: A process study on thinning of Arctic winter cirrus clouds with high-resolution ICON-ART simulations, J. Geophys. Res., 124, 5860–5888, https://doi.org/10.1029/2018JD029815, 2019.

Gryspeerdt, E., Sourdeval, O., Quaas, J., Delanoë, J., Krämer, M., and Kühne, P.: Ice crystal number concentration estimates from lidar–radar satellite remote sensing – Part 2: Controls on the ice crystal number concentration, Atmos. Chem. Phys., 18, 14351–14370, https://doi.org/10.5194/acp-18-14351-2018, 2018.

Haag, W., Kärcher, B., Ström, J., Minikin, A., Lohmann, U., Ovarlez, J., and Stohl, A.: Freezing thresholds and cirrus cloud formation mechanisms inferred from in situ measurements of relative humidity, Atmos. Chem. Phys., 3, 1791–1806, https://doi.org/10.5194/acp-3-1791-2003, 2003.

Hoffmann, L., Grimsdell, A. W., and Alexander, M. J.: Stratospheric gravity waves at Southern Hemisphere orographic hotspots: 2003–2014 AIRS/Aqua observations, Atmos. Chem. Phys., 16, 9381–9397, https://doi.org/10.5194/acp-16-9381-2016, 2016.

Hong, Y., Liu, G., and Li, J. F.: Assessing the radiative effects of global ice clouds based on CloudSat and CALIPSO measurements, J. Climate, 29, 7651–7674, https://doi.org/10.1175/JCLI-D-15-0799.1, 2016.

Hu, Y., McFarquhar, G. M., Wu, W., Huang, Y., Schwarzenboeck, A., Protat A., Korolev, A., Rauber, R., and Wang, H.: Dependence of Ice Microphysical Properties on Environmental Parameters: Results from HAIC-HIWC Cayenne Field Campaign, J. Atmos. Sci., 78, 2957–2981, https://doi.org/10.1175/JAS-D-21-0015.1, 2021.

Jackson, L. S., Crook, J. A., and Forster, P. M.: An intensified hydrological cycle in the simulation of geoengineering by cirrus cloud thinning using ice crystal fall speed changes, J. Geophys. Res.-Atmos., 121, 6822–6840, https://doi.org/10.1002/2015JD024304, 2016.

Jensen, E. J., Pfister, L., and Bui, T. P.: Physical processes controlling ice concentrations in cold cirrus near the tropical tropopause, J. Geophys. Res., 117, D11205, https://doi.org/10.1029/2011JD017319, 2012.

Jensen, E. J., Kärcher, B., Woods, S., Krämer, M., and Ueyama, R.: The impact of gravity waves on the evolution of tropical anvil cirrus microphysical properties, J. Geophys. Res., 129, e2023JD039887, https://doi.org/10.1029/2023JD039887, 2024.

Jiang, J., Wu, D. L., and Eckermann, S. D.: Upper Atmospheric Research Satellite (UARS) MLS observation of mountain waves over the Andes, J. Geophys. Res., 107, 8273, https://doi.org/10.1029/2002JD002091, 2002.

Joos, H., Spichtinger, P., Lohmann, U., Gayet, J.-F., and Minikin, A.: Orographic cirrus in the global climate model ECHAM5, J. Geophys. Res., 113, D18205, https://doi.org/10.1029/2007JD009605, 2008.

Joos, H., Spichtinger, P., Reutter, P., and Fusina, F.: Influence of heterogeneous freezing on the microphysical and radiative properties of orographic cirrus clouds, Atmos. Chem. Phys., 14, 6835–6852, https://doi.org/10.5194/acp-14-6835-2014, 2014.

Kiehl, J. T. and Trenberth, K. E.: Earth's annual global mean energy budget, B. Am. Meteorol. Soc., 78, 197–208, https://doi.org/10.1175/1520-0477(1997)078<197:EAGMEB>2.0.CO;2, 1997.

Kok, J. F., Adebiyi, A. A., Albani, S., Balkanski, Y., Checa-Garcia, R., Chin, M., Colarco, P. R., Hamilton, D. S., Huang, Y., Ito, A., Klose, M., Leung, D. M., Li, L., Mahowald, N. M., Miller, R. L., Obiso, V., Pérez García-Pando, C., Rocha-Lima, A., Wan, J. S., and Whicker, C. A.: Improved representation of the global dust cycle using observational constraints on dust properties and abundance, Atmos. Chem. Phys., 21, 8127–8167, https://doi.org/10.5194/acp-21-8127-2021, 2021.

Koop, T., Luo, B., Tsias, A., and Peter, T.: Water activity as the determinant for homogeneous ice nucleation in aqueous solutions, Nature, 406, 611–614, https://doi.org/10.1038/35020537, 2000.

Krämer, M., Rolf, C., Luebke, A., Afchine, A., Spelten, N., Costa, A., Meyer, J., Zöger, M., Smith, J., Herman, R. L., Buchholz, B., Ebert, V., Baumgardner, D., Borrmann, S., Klingebiel, M., and Avallone, L.: A microphysics guide to cirrus clouds – Part 1: Cirrus types, Atmos. Chem. Phys., 16, 3463–3483, https://doi.org/10.5194/acp-16-3463-2016, 2016.

Krämer, M., Rolf, C., Spelten, N., Afchine, A., Fahey, D., Jensen, E., Khaykin, S., Kuhn, T., Lawson, P., Lykov, A., Pan, L. L., Riese, M., Rollins, A., Stroh, F., Thornberry, T., Wolf, V., Woods, S., Spichtinger, P., Quaas, J., and Sourdeval, O.: A microphysics guide to cirrus – Part 2: Climatologies of clouds and humidity from observations, Atmos. Chem. Phys., 20, 12569–12608, https://doi.org/10.5194/acp-20-12569-2020, 2020.

Kristjánsson, J. E., Muri, H., and Schmidt, H.: The hydrological cycle response to cirrus cloud thinning, Geophys. Res. Lett., 42, 10807–10815, https://doi.org/10.1002/2015GL066795, 2015.

Lamb, D. and Verlinde, J.: Physics and chemistry of clouds, Cambridge University Press, https://doi.org/10.1017/CBO9780511976377, 2011.

Lin, L., Liu, X., Zhao, X., Shan, Y., Ke, Z., Lyu, K., and Bowman, K. P.: Ice nucleation by volcanic ash greatly alters cirrus cloud properties, Sci. Adv., 11, eads0572, https://doi.org/10.1126/sciadv.ads0572, 2025.

Liu, X. H. and Penner, J. E.: Ice nucleation parameterization for global models, Meteorol. Z., 14, 499–514, https://doi.org/10.1127/0941-2948/2005/0059, 2005.

Liu, X., Shi, X., Zhang, K., Jensen, E. J., Gettelman, A., Barahona, D., Nenes, A., and Lawson, P.: Sensitivity studies of dust ice nuclei effect on cirrus clouds with the Community Atmosphere Model CAM5, Atmos. Chem. Phys., 12, 12061–12079, https://doi.org/10.5194/acp-12-12061-2012, 2012.

Liu, J. and Shi, X.: Estimating the potential cooling effect of cirrus thinning achieved via the seeding approach, Atmos. Chem. Phys., 21, 10609–10624, https://doi.org/10.5194/acp-21-10609-2021, 2021.

Lohmann, U. and Gasparini, B.: A cirrus cloud climate dial?, Science, 357, 248–249, https://doi.org/10.1126/science.aan3325, 2017.

Luebke, A. E., Afchine, A., Costa, A., Grooß, J.-U., Meyer, J., Rolf, C., Spelten, N., Avallone, L. M., Baumgardner, D., and Krämer, M.: The origin of midlatitude ice clouds and the resulting influence on their microphysical properties, Atmos. Chem. Phys., 16, 5793–5809, https://doi.org/10.5194/acp-16-5793-2016, 2016.

Lüttmer, T., Miltenberger, A., and Spichtinger, P.: On the impact of ice formation processes and sedimentation on cirrus origin classification in warm conveyor belt outflow, Atmos. Chem. Phys., 25, 10245–10265, https://doi.org/10.5194/acp-25-10245-2025, 2025.

Lyu, K., Liu, X., Bacmeister, J., Zhao, X., Lin, L., Shi, Y., and Sourdeval, O.: Orographic cirrus and its radiative forcing in NCAR CAM6, J. Geophys. Res.-Atmos., 128, e2022JD038164, https://doi.org/10.1029/2022JD038164, 2023.

Matus, A. V. and L'Ecuyer, T. S.: The role of cloud phase in Earth's radiation budget, J. Geophys. Res., 122, 2559–2578, https://doi.org/10.1002/2016JD025951, 2017.

McCluskey, C. S., Hill, T. C. J., Humphries, R. S., Rauker, A. M., Moreau, S., Strutton, P. G., Chambers, S. D., Williams, A. G., McRobert, I., Ward, J., Keywood, M. D., Harnwell, J., Ponsonby, W., Loh, Z. M., Krummel, P. B., Protat, A., Kreidenweis, S. M., and DeMott, P. J.: Observations of ice nucleating particles over Southern Ocean waters, Geophys. Res. Lett., 45, 11989–11997, https://doi.org/10.1029/2018GL079981, 2018.

Mishra, S., Mitchell, D. L., Turner, D. D., and Lawson, R. P.: Parameterization of ice fall speeds in midlatitude cirrus: results from SPartICus, J. Geophys. Res.-Atmos., 119, 3857–3876, https://doi.org/10.1002/2013jd020602, 2014.

Mitchell, D. L.: Evolution of snow-size spectra in cyclonic storms. Part I: Snow growth by vapor deposition and aggregation, J. Atmos. Sci., 45, 3431–3451, https://doi.org/10.1175/1520-0469(1988)045<3431:EOSSSI>2.0.CO;2, 1988.

Mitchell, D. L.: A model predicting the evolution of ice particle size spectra and radiative properties of cirrus clouds. Part 1: Microphysics, J. Atmos. Sci., 51, 797–816, https://doi.org/10.1175/1520-0469(1994)051<0797:AMPTEO>2.0.CO;2, 1994.

Mitchell, D. L. and Finnegan, W.: Modification of cirrus clouds to reduce global warming, Environ. Res. Lett., 4, 045102, https://doi.org/10.1088/1748-9326/4/4/045102, 2009.

Mitchell, D. L, Ivanova, D., Edwards, J. M., and McFarquhar, G. C.: A GCM parameterization of bimodal size spectral for ice clouds, in: Ninth ARM Science Team Meeting Proceedings, San Antonio, Texas, 22–26 March 1999, https://www.arm.gov/publications/proceedings/conf09/extended_abs/mitchell2_dl.pdf (last access: 31 October 2024), 1999.

Mitchell, D. L., Rasch, P., Ivanova, D., McFarquhar, G., and Nousiainen, T.: Impact of small ice crystal assumptions on ice sedimentation rates in cirrus clouds and GCM simulations, Geophys. Res. Lett., 35, L09806, https://doi.org/10.1029/2008GL033552, 2008.

Mitchell, D. L. and d'Entremont, R. P.: Satellite retrieval of the liquid water fraction in tropical clouds between −20 and −38 °C, Atmos. Meas. Tech., 5, 1683–1698, https://doi.org/10.5194/amt-5-1683-2012, 2012.

Mitchell, D. L., Garnier, A., Pelon, J., and Erfani, E.: CALIPSO (IIR–CALIOP) retrievals of cirrus cloud ice-particle concentrations, Atmos. Chem. Phys., 18, 17325–17354, https://doi.org/10.5194/acp-18-17325-2018, 2018.

Mitchell, D. L., Mejia, J., Garnier, A., Tomii, Y., Krämer, M., and Hosseinpour, F.: An Estimate of Global, Regional and Sea-

sonal Cirrus Cloud Radiative Effects Contributed by Homogeneous Ice Nucleation, Atmos. Chem. Phys. Discuss. [preprint], https://doi.org/10.5194/acp-2020-846, 2020.

Mitchell, D. L., Garnier, A., and Woods, S.: Advances in CALIPSO (IIR) cirrus cloud property retrievals – Part 1: Methods and testing, Atmos. Chem. Phys., 25, 14071–14098, https://doi.org/10.5194/acp-25-14071-2025, 2025.

Muench, S. and Lohmann, U.: Developing a cloud scheme with prognostic cloud fraction and two moment microphysics for ECHAM-HAM, J. Adv. Model. Earth Sy., 12, e2019MS001824, https://doi.org/10.1029/2019MS001824, 2020.

Muri, H., Kristjánsson, J. E., Storelvmo, T., and Pfeffer, M. A.: The climatic effects of modifying cirrus clouds in a climate engineering framework, J. Geophys. Res., 119, 4174–4191, https://doi.org/10.1002/2013JD021063, 2014.

Muri, H., Tjiputra, J., Otterå, O. H., Adakudlu, M., Lauvset, S. K., Grini, A., Schulz, M., Niemeier, U., and Kristjánsson, J. K.: Climate response to aerosol geoengineering: A multimethod comparison, J. Climate, 31, 6319–6340, https://doi.org/10.1175/JCLI-D-17-0620.1, 2018.

Ngo, D., Diao, M., Patnaude, R. J., Woods, S., and Diskin, G.: Aerosol Indirect Effects on Cirrus Clouds Based on Global-Scale Airborne Observations and Machine Learning Models, EGUsphere [preprint], https://doi.org/10.5194/egusphere-2024-2122, 2024.

NASA/LARC/SD/ASDC: CALIPSO Infrared Imaging Radiometer (IIR) Level 2 Track, V4-51, NASA Langley Atmospheric Science Data Center DAAC [data set], https://doi.org/10.5067/IIR/CALIPSO/CAL_IIR_L2_Track-Standard-V4-51, 2023a.

NASA/LARC/SD/ASDC: CALIPSO Lidar Level 2 Cloud Profile, V4-51, NASA Langley Atmospheric Science Data Center DAAC [data set], https://doi.org/10.5067/CALIOP/CALIPSO/CAL_LID_L2_05kmCPro-Standard-V4-51, 2023b.

Patnaude, R. and Diao, M.: Aerosol Indirect Effects on Cirrus Clouds Based on Global Aircraft Observations, Geophys. Res. Lett., 47, e2019GL086550, https://doi.org/10.1029/2019GL086550, 2020.

Penner, J. E., Zhou, C., and Liu, X.: Can cirrus cloud seeding be used for geoengineering?, Geophys. Res. Lett., 42, 8775–8782, https://doi.org/10.1002/2015GL065992, 2015.

Rosenfeld, D. and Woodley, W.: Deep convective clouds with sustained supercooled liquid water down to −37.5 °C, Nature, 405, 440–442, https://doi.org/10.1038/35013030, 2000.

Schneider, J., Höhler, K., Wagner, R., Saathoff, H., Schnaiter, M., Schorr, T., Steinke, I., Benz, S., Baumgartner, M., Rolf, C., Krämer, M., Leisner, T., and Möhler, O.: High homogeneous freezing onsets of sulfuric acid aerosol at cirrus temperatures, Atmos. Chem. Phys., 21, 14403–14425, https://doi.org/10.5194/acp-21-14403-2021, 2021.

Shi, X., Liu, X., and Zhang, K.: Effects of pre-existing ice crystals on cirrus clouds and comparison between different ice nucleation parameterizations with the Community Atmosphere Model (CAM5), Atmos. Chem. Phys., 15, 1503–1520, https://doi.org/10.5194/acp-15-1503-2015, 2015.

Song, Q., Zhang, Z., Yu, H., Ginoux, P., and Shen, J.: Global dust optical depth climatology derived from CALIOP and MODIS aerosol retrievals on decadal timescales: regional and interannual variability, Atmos. Chem. Phys., 21, 13369–13395, https://doi.org/10.5194/acp-21-13369-2021, 2021.

Sourdeval, O., Gryspeerdt, E., Krämer, M., Goren, T., Delanoë, J., Afchine, A., Hemmer, F., and Quaas, J.: Ice crystal number concentration estimates from lidar–radar satellite remote sensing – Part 1: Method and evaluation, Atmos. Chem. Phys., 18, 14327–14350, https://doi.org/10.5194/acp-18-14327-2018, 2018.

Spichtinger, P. and Gierens, K. M.: Modelling of cirrus clouds – Part 1a: Model description and validation, Atmos. Chem. Phys., 9, 685–706, https://doi.org/10.5194/acp-9-685-2009, 2009a.

Spichtinger, P. and Gierens, K. M.: Modelling of cirrus clouds – Part 1b: Structuring cirrus clouds by dynamics, Atmos. Chem. Phys., 9, 707–719, https://doi.org/10.5194/acp-9-707-2009, 2009b.

Sporre, M. K., Friberg, J., Svenhag, C., Sourdeval, O., and Storelvmo, T.: Springtime stratospheric volcanic aerosol impact on midlatitude cirrus clouds, Geophys. Res. Lett., 49, e2021GL096171, https://doi.org/10.1029/2021GL096171, 2022.

Stephens, G. L.: Cloud feedbacks in the climate system: A critical review, J. Climate, 18, 237–273, https://doi.org/10.1175/JCLI-3243.1, 2005.

Storelvmo, T., Kristjansson, J. E., Muri, H., Pfeffer, M., Barahona, D., and Nenes, A.: Cirrus cloud seeding has potential to cool climate, Geophys. Res. Lett., 40, 178–182, https://doi.org/10.1029/2012GL054201, 2013.

Storelvmo, T. and Herger, N.: Cirrus cloud susceptibility to the injection of ice nuclei in the upper troposphere, J. Geophys. Res.-Atmos., 119, 2375–2389, https://doi.org/10.1002/2013JD020816, 2014.

Storelvmo, T., Boos, W. R., and Herger, N.: Cirrus cloud seeding: a climate engineering mechanism with reduced side effects?, Philos. T. Roy. Soc. A, 372, 20140116, https://doi.org/10.1098/rsta.2014.0116, 2014.

Tully, C., Neubauer, D., Omanovic, N., and Lohmann, U.: Cirrus cloud thinning using a more physically based ice microphysics scheme in the ECHAM-HAM general circulation model, Atmos. Chem. Phys., 22, 11455–11484, https://doi.org/10.5194/acp-22-11455-2022, 2022.

Tully, C., Neubauer, D., Villanueva, D., and Lohmann, U.: Does prognostic seeding along flight tracks produce the desired effects of cirrus cloud thinning?, Atmos. Chem. Phys., 23, 7673–7698, https://doi.org/10.5194/acp-23-7673-2023, 2023.

United Nations Environment Programme: One Atmosphere: An independent expert review on Solar Radiation Modification research and deployment, Kenya, Nairobi, https://wedocs.unep.org/handle/20.500.11822/41903 (last access: 9 October 2025), 2023.

Vergara-Temprado, J., Miltenberger, A. K., Furtado, K., Grosvenor, D. P., Shipway, B. J., Hill, A. A., Wilkinson, J. M., Field, P. R., Murray, B. J., and Carslaw, K. S.: Strong control of Southern Ocean cloud reflectivity by ice-nucleating particles, P. Natl. Acad. Sci. USA, 115, 2687–2692, https://doi.org/10.1073/pnas.1721627115, 2018.

Wernli, H., Boettcher, M., Joos, H., Miltenberger, A. K., and Spichtinger, P.: A trajectory-based classification of ERA-Interim ice clouds in the region of the North Atlantic storm track, Geophys. Res. Lett., 43, 6657–6664, https://doi.org/10.1002/2016GL068922, 2016.